



HAL
open science

Effect of hardening on toughness captured by stress-based damage nucleation in 6061 aluminum alloy

Tom Petit, Jacques Besson, Claire Ritter, Kimberly Colas, Lukas Helfen,
Thilo F. Morgeneyer

► To cite this version:

Tom Petit, Jacques Besson, Claire Ritter, Kimberly Colas, Lukas Helfen, et al.. Effect of hardening on toughness captured by stress-based damage nucleation in 6061 aluminum alloy. *Acta Materialia*, 2019, 180, pp.349-365. 10.1016/j.actamat.2019.08.055 . hal-02307867

HAL Id: hal-02307867

<https://hal.science/hal-02307867v1>

Submitted on 9 Oct 2019

HAL is a multi-disciplinary open access archive for the deposit and dissemination of scientific research documents, whether they are published or not. The documents may come from teaching and research institutions in France or abroad, or from public or private research centers.

L'archive ouverte pluridisciplinaire **HAL**, est destinée au dépôt et à la diffusion de documents scientifiques de niveau recherche, publiés ou non, émanant des établissements d'enseignement et de recherche français ou étrangers, des laboratoires publics ou privés.

Effect of hardening on toughness captured by stress-based damage nucleation in 6061 aluminum alloy

Tom Petit^{1,2,*}, Jacques Besson², Claire Ritter¹, Kimberly Colas¹, Lukas Helfen^{3,4}, Thilo F. Morgeneyer²

¹ DEN-Service d'Etudes des Matériaux Irradiés, CEA, Université Paris-Saclay, F-91191, Gif-sur-Yvette, France

² MINES ParisTech, PSL Research University, Centre des matériaux, CNRS UMR 7633, France

³ Institute for Photon Science and Synchrotron Radiation, Karlsruhe Institute of Technology (KIT), Germany

⁴ European Synchrotron Radiation Facility (ESRF), Grenoble, France

Abstract

A deterioration of fracture toughness, especially of the tearing modulus, with aging time and associated strength increase is observed for aluminum 6061 and reproduced here numerically thanks to a stress-based damage nucleation criterion.

A correlative multiscale analysis by scanning electron microscopy, atom probe tomography as well as 3D X-ray laminography shows that coarse particles and the characteristic damage mechanisms do not depend on aging time: the fracture mechanism is typically ductile and transgranular as shown by electron backscatter diffraction analysis of sections of compact tension specimens containing interrupted cracks. Large Mg₂Si inclusions fracture at very low plastic strain, and defects nucleate at large (Fe,Si)-rich inclusions with increasing plastic deformation. Only the hardening nanoprecipitation increases with aging time: aging favors the precipitation of nano-size Mg₂Si precipitates which causes hardening of the matrix so that damage nucleation at coarse inclusions becomes easier - thus leading to a decrease in toughness. Indeed, larger clusters and a substantially higher area fraction of iron based intermetallic particles are found on the fracture surfaces of the longest aging time CT samples compared to the shortest aging time samples.

Based on these observations, a Gurson-Tvergaard Needleman type model is proposed to simulate the tearing tests using Finite Elements. It uses damage nucleation kinetics which depend on the maximum principal stress, since a classical strain-based nucleation is not sufficient to reproduce the deterioration of the tearing modulus.

Keywords: Fracture mechanisms; Toughness; Ductile fracture, Nucleation; Aluminum alloys

* Corresponding author

E-mail address: tom.petit@cea.fr (T. Petit)

1. Introduction

The in-depth understanding of the relationship between the processing, the structure and the properties of material is key to elaborate innovative materials. A multi-scale approach is necessary to understand the influence of the microstructure on macroscopic mechanical properties, especially on tearing resistance. With the current knowledge of the community, given the material microstructure and its tensile properties, fracture toughness of a given material can still not be predicted.

The present study aims at understanding the link between microstructure evolutions during aging, strength evolutions and associated toughness changes in order to be able to optimize microstructures by modelling and to predict its mechanical properties.

In the literature, a decrease of toughness with increasing yield stress has been identified by Dumont et al. [1–3]. For 7040 and 7050 alloys, strength increases during aging up to the peak-aged condition and subsequently decreases. The associated toughness drops with increasing strength and rises again for the over-aged state, but not to the same level as for the under-aged condition. The reduction of toughness after peak-aged has been attributed to a lower hardening capacity of the material compared to an under-aged condition with the same yield stress. Dumont et al. explain the toughness decrease by the increasing fraction of intergranular fracture, which is governed by the strength ratio between the Precipitate Free Zone (PFZ) at grain boundaries and the matrix. They identified more shear fracture on the under-aged state and more intergranular fracture for the over-aged state for the fast quench material. They modelled the toughness evolution as a function of aging by accounting for the PFZ stress. Ryum [4,5] et Ludtka et al. [6] showed similar results for 7XXX aluminum alloys series.

Hannard [7] studied the ductility evolution with aging for three AA6XXX aluminum alloys. This ductility decreases with yield stress increase. They reproduced this evolution using a nucleation-growth-coalescence model with a dedicated nucleation model, which uses stress-based criterion linked with Weibull size distribution.

Other authors [8,9] investigated the effect of quench rate on toughness for 6061 aluminum. A high quench rate reduced the PFZ size, which was accompanied by an increase in toughness and less intergranular fracture. For a high quench rate applied to 6061 aluminum in T6 condition, Shen et al. [10] showed that rupture is classically ductile. Using laminography technique, they concluded that coarse Mg_2Si particles break at a lower strain level than InterMetallic (IM) particles, which are secondary preferential nucleation sites.

In a previous study [11] by the present authors, a decrease in toughness was observed with aging time in a 6061 aluminum alloy after aging at 175 °C during 4, 8, 12 or 16 h. Aging causes hardening and toughness drop (Figure 1). During toughness tests, the drop in load after the maximum load depends on the material crack growth toughness (which is quantified by the tearing modulus calculation): the faster the load decreases, the faster the crack propagates. The decrease in toughness with aging time is therefore clearly identifiable in Figure 1. It is fundamental to understand whether this decrease results from a change in the coarse particles (responsible for the damage), or in the fracture mechanisms, or whether it is solely due to the hardening of the matrix observed in tensile tests.

The objective of the current work is to capture numerically this evolution of toughness. Increasing strength and decreasing hardening will be accounted for using fitted hardening curves (dotted lines in Figure 1). Therefore, the plastic zone size will naturally evolve for the different simulated configurations.

To the best of our knowledge, there is no simulation using a Gurson-Tvergaard-Needleman (GTN) model able to capture the effect of aging time on tearing resistance. The GTN model is a void growth model; for nucleation, the model proposed by Chu and Needleman [12] is classically used. In other works, nucleation has been based on stress triaxiality state [13] or on Lode parameter for shear deformation states and reproduction of slant fracture [14,15]. Strain and stress based nucleation criteria have also been suggested in Needleman and Rice [16] and in Butcher et al. [17].

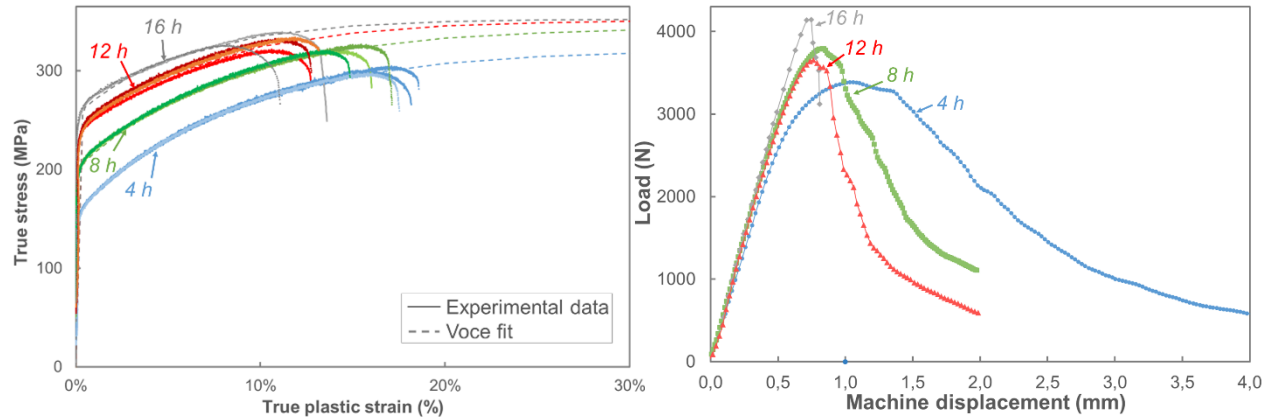


Figure 1 – Experimental tensile curves (and fitted curves) on the left, CT-toughness test curves (load as a function of machine displacement) on the right for the four aging times (4, 8, 12 or 16 h) [11]

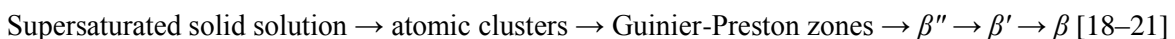
The objective of this work is to identify the micromechanistic origin of the toughness evolution as a function of aging time and to capture this evolution using the GTN model. The paper is organized as follows:

- Description of experimental methods in section 2.
- Study of undamaged material and the effect of aging on the microstructure in section 3.1, using Scanning Electron Microscopy (SEM) for coarse particle analysis, Electron Backscatter Diffraction (EBSD) for grain distribution investigation, and Atom Probe Tomography (APT) for hardening nanoprecipitation evolution study.
- Fracture mechanisms as a function of aging state are identified in section 3.2 using fractography, laminography and EBSD of section containing interrupted cracks, in order to identify transgranular and intergranular fracture.
- Simulation of decrease in toughness based on the identified damage mechanisms using a stress-based nucleation model in section 4.

2. Experimental methods

2.1. Material

The material used in this study is an aluminum alloy 6061(Al-Mg-Si), as received in a T6 condition (homogenization, hot forging, solution annealing, water quenching and isothermal aging heat treatments). The ingot material was hot-worked to produce uniform grains and close porosities along three directions X, Y and Z. The chemical composition is given in the Table 1. The age-hardening state allows us to obtain various metallurgical states and various mechanical behaviors by modifying only aging treatments: the strength is linked to the precipitation of nano-scaled β'' -Mg₂Si phases during aging (heat treatment at 175 °C). More generally, the Al-Mg-Si alloy family decomposes from the supersaturated solid solution according to the following sequence:



Si	Mg	Fe	Cr	Cu	Mn	Zn	Ti	Ni	Zr	Pb	Na	Al
0.53	1.08	0.38	0.18	0.22	0.06	0.22	0.02	0.0045	0.0038	0.0021	0.0001	bal.

Table 1 –Chemical composition (% by weight) of the 6061 alloy studied

The as-received reference material was first solution treated (at 550 °C for 4 hours), and then age-hardened at 175 °C during four aging times (4, 8, 12 and 16 hours) using four material blocks (136 x 76 x 87 mm³) to produce different mechanical behaviors. The objective is to characterize the microstructure of the undamaged material, to determine whether or not the aging process could have created weak metallurgical zones, causing the decrease in toughness.

The cylindrical tensile specimens (gage length of 26 mm, diameter of 4 mm) and Compact Tension (CT) specimens (thickness 12.5 mm, width 25 mm) were machined from these blocks along the same direction for each heat treatment (tensile direction along Z). Samples for microstructural investigations were coated, polished (successively with SiC abrasive paper, diamond paste up to 1 μm, finally with OP-S pH 11 during 3 min), cleaned (first with soap and water, secondly with distilled water then ethanol in an ultrasonic bath) and chemically etched with an etchant referred to as Keller's reagent (95 % water, 2.5 % HNO₃, 1.5 % HCl, 1 % HF).

2.2. Scanning Electron Microscopy (SEM)

The used SEM is a JEOL IT300 which is equipped with an EBSD (Electron Backscatter Diffraction) detector NordlysMax³. The observations were performed in the three observation planes: XY, XZ and YZ. Tensile tests had been carried out according to the Z axis, and fracture toughness tests according to the Z axis with a crack propagation along X. A grain boundary is considered when the misorientation angle between the two grains affected is at least equal to 15° [22]. A sub-structure consisting of some sub-grains could be identified by considering sub-boundaries of grains corresponding to a misorientation angle between 5° and 15°.

Fractographic analyses of fracture surfaces of CT samples after fracture toughness tests were realized through an FEI Nova NanoSEM 450 with a secondary electron detector and a backscattered electron detector, enabled to qualify damage micromechanisms. To quantify the area fractions of iron-rich intermetallic particles on the 4 h aged material, 7 areas of the size of Figure 6 c were segmented using a gray value threshold. For the 16 h aged material, 8 areas of the size of Figure 6 d were used. This corresponded to areas of about 10 mm². It is completed by an energy dispersive X-ray spectroscopy (EDS) detector X-MAS^N allowing one to identify precipitates.

2.3. Atom Probe Tomography (APT)

Samples preparation and experimental protocols are described by Buchanan et al. [23].

Rods of 0.3 mm of side were then mechanically cut from two blocks aged during respectively 4 and 12 h and atom probe samples (needle-shape specimens with an end-radius on the order of 50-100 nm) were prepared by a standard electro-polishing method using two successive solutions: 70% methanol - 30% nitric acid, then 98% 2-butoxyethanol - 2% perchloric acid at room temperature.

The 3D Atom Probe analyses were performed with the CAMECA LEAP 4000X HR in an ultra-high vacuum and at cryogenic temperatures. The specimen is held at high voltage and atoms at the end surface of the needle-shaped specimen are field evaporated through application of a time voltage pulse. Evaporated ions are then accelerated by the local electric field to finally hit a position sensitive detector. Hit positions of incident ions and time of incidence information are converted respectively to reconstruct individual ions positions and specimen geometries and to identify individual elements and isotopes based on mass-to-charge ratios. The parameters of APT analyses are described in the Table 2.

Mode	Temperature	Pressure	Detection rate	Pulse fraction	Background	Standing voltage
	K	10 ⁻¹⁰ torr	%	%	ppm/nsec	V
Voltage	44-47	0.4-1.0	0.4-0.6	18	16-35	2900-7200

Table 2 - Parameters of APT analyses

The data processing was realized with the data treatment software IVAS 3.6.12 from CAMECA. For the three specimens studied in this paper, calibration of the reconstruction parameters was performed by using cylindrical volumes to isolate the $\langle 022 \rangle_{Al}$ zone axis and adjusting the image compression factor (ICF) and K factor to obtain good agreement between the zones expected and measured inter-planar spacings. Optimization of the ICF and K parameters to minimize the curvature of the atomic planes was performed using the method described in [24].

2.4. Laminography

Synchrotron-radiation computed tomography (SRCT) is particularly relevant for the fast high-resolution imaging of one-dimensionally elongated, i.e. matchstick-like, specimens, which stay during rotation inside the field of view of the detector system. In contrast, synchrotron-radiation computed laminography (SRCL) [25,26] enables the imaging of regions of interest in flat samples (like microelectronic devices or alloy sheet materials). In this study, we employ this three-dimensional nondestructive examination with high spatial resolution in order to analyze the damage state and the evolution of the damage in the volume of the material. Laminography consists in tilting the rotation axis, which is perpendicular to the transmitted beam for SRCT, by an angle between 0 and 90°. When the specimen plane is oriented approximately perpendicular to the rotation axis, we can obtain a similar X-ray transmission for a complete 360° rotation resulting in more reliable projection data compared to SRCT. The experimental methods are described in more detail in [27]. The 2D projections are used to reconstruct a 3D image of the sample at the region of interest using a filtered-backprojection algorithm [28,29]. Crack propagation in aluminum alloys have already been successfully studied with this technique [10,14,30].

Imaging was performed on KIT's laminography instrument installed at beamline ID19 [31] of the European Synchrotron Radiation Facility (ESRF), Grenoble, France. The axis tilt angle was chosen around $\theta=65^\circ$. A pink beam with an X-ray energy around 26 keV [14] allows a good compromise between penetration and depth resolution. This allowed us to distinguish Mg₂Si inclusions and aluminum matrix. 3599 projections, with an exposure time of 37 ms each, enable to build a volume. The final reconstructed volumes have a size of 2560x2560x2300 voxels with a voxel size of 0.65 μm .

In order to study the fracture mechanism, 2D cuts and 3D visualizations of reconstructed laminography data containing cracks were performed. The ImageJ software (<https://imagej.nih.gov/ij/>) allowed us to select interest areas, and then the AnalySIS software (<https://www.olympus-ims.com/fr/microscope/software/>) enabled us to overlay all the images, in order to obtain large 2D cuts in two observation directions. The 3D visualization of damage was performed through the software Avizo 3D. As the contrast between the aluminum matrix and the void of the crack was too low, the watershed algorithm enabled to improve the detection of the edges of contrasted areas.

We also performed nanolaminography [32] on two selected samples in order to provide 3D images of the microstructure at the sub- μm scale. The nanolaminography scans shown in Figure 3 were performed at ESRF beamline ID16b, which is dedicated to 3D nano-scale imaging. Using a projection microscopy approach allows us to improve the spatial resolution towards voxel sizes of 100 nm in a $216 \times 216 \times 200 \mu\text{m}^3$ volume.

3. Experimental results

The aim of this microstructural study is to identify the material microstructure and its evolution due to aging time. The damage micromechanisms are also identified as a function of aging time.

3.1. Microstructure of different age-hardened material

3.1.1. Grains and coarse particles

The two kinds of coarse particles are Mg_2Si (small dark-grey features in Figure 2) and (Fe,Si)-rich intermetallics (long gray filaments) denoted IM. The mean diameter of a Mg_2Si particle is $5 \mu\text{m}$ and the mean length of an IM particle is $244 \mu\text{m}$. Following Shen [10], Mg_2Si will be assumed to debond for very low levels of plastic strain, so that the volume fraction can be considered as part of the initial void volume fraction. The mean surface fractions are respectively 0.35 % and 2.15 % for the Mg_2Si + initial pores and the IM. It was checked that both surface fractions are equal to volume fractions for the 8 hours aged material.

As shown in Figure 2 *c* and *d* (black lines are the grain boundaries, blue lines are the sub-boundaries), no preferential localization is observed at the grain boundaries: contrary to what Shen et al. [10,33] had shown, coarse particles are mostly integrated in grains, and does not necessarily follow grain boundaries. However, it is noted that the small grains are strongly disoriented (as the strong presence of subgrain boundaries attests), and that the particles tend to be located at the boundaries of these small grains, as shown in Figure 2 *b* and *f*. The IMs appear evenly distributed, contrary to the clusters of clusters distribution shown by Hannard et al. [34] along the rolling direction for their rolled material. The Mg_2Si particles are gathered into clusters (Figure 3). All these observations and these parameters concerning the coarse particles do not depend on aging time.

The typical grain distribution is shown in Figure 4. These EBSD maps are in the XY plane to show the geometrical grain orientation: the grains are elongated along the X and Y axes with a 45° angle and a 2.9 form factor. Two grain populations can be identified: large grains cover 72 % of the surface with a mean equivalent diameter of $1014 \mu\text{m}$, smaller grains cover 28 % with a mean equivalent diameter of $287 \mu\text{m}$. The grain distribution and the quantified parameters introduced above do not depend on aging time.

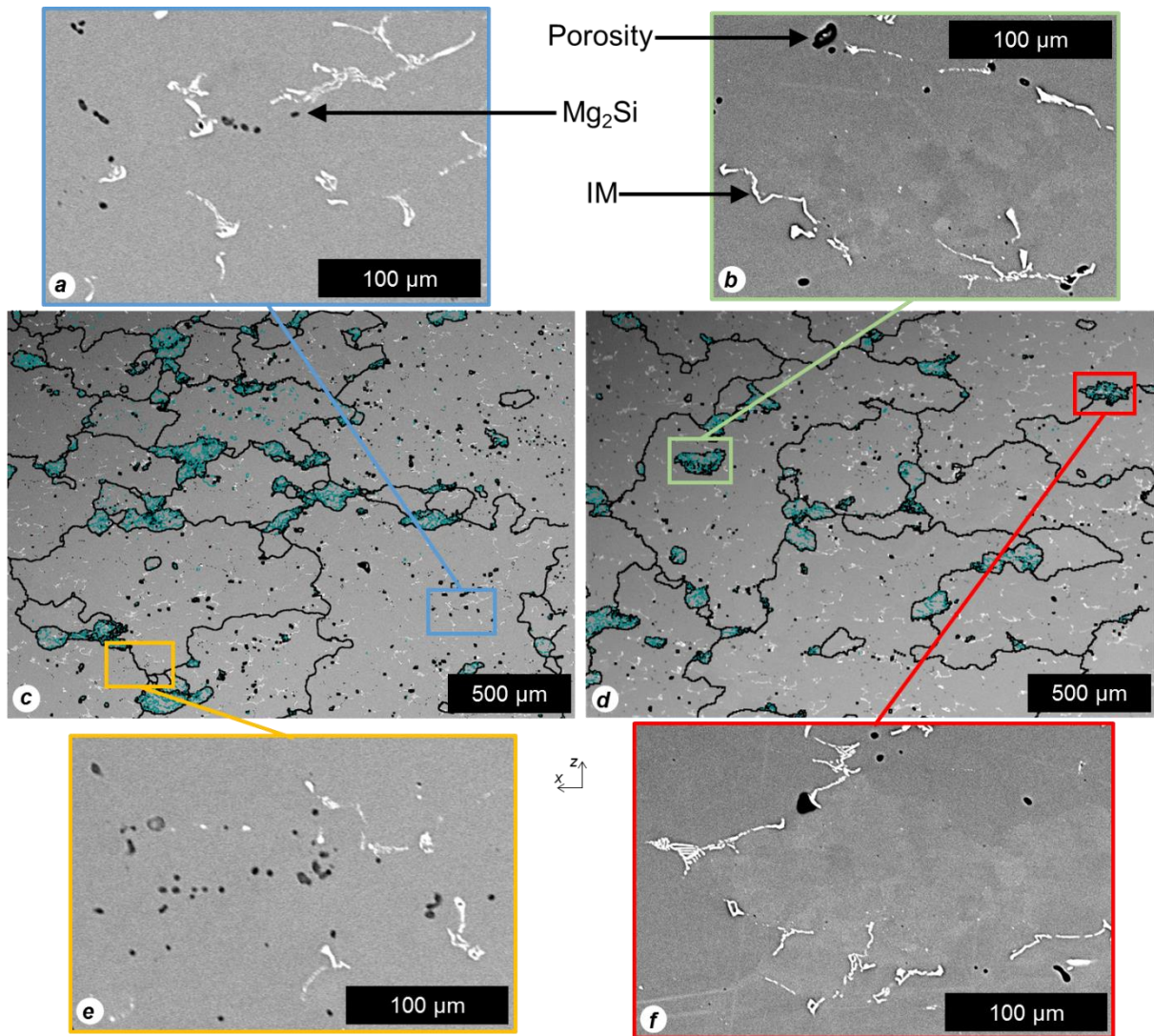


Figure 2 – Coarse precipitation localization after 12 h aging (SEM micrographs of polished sections)

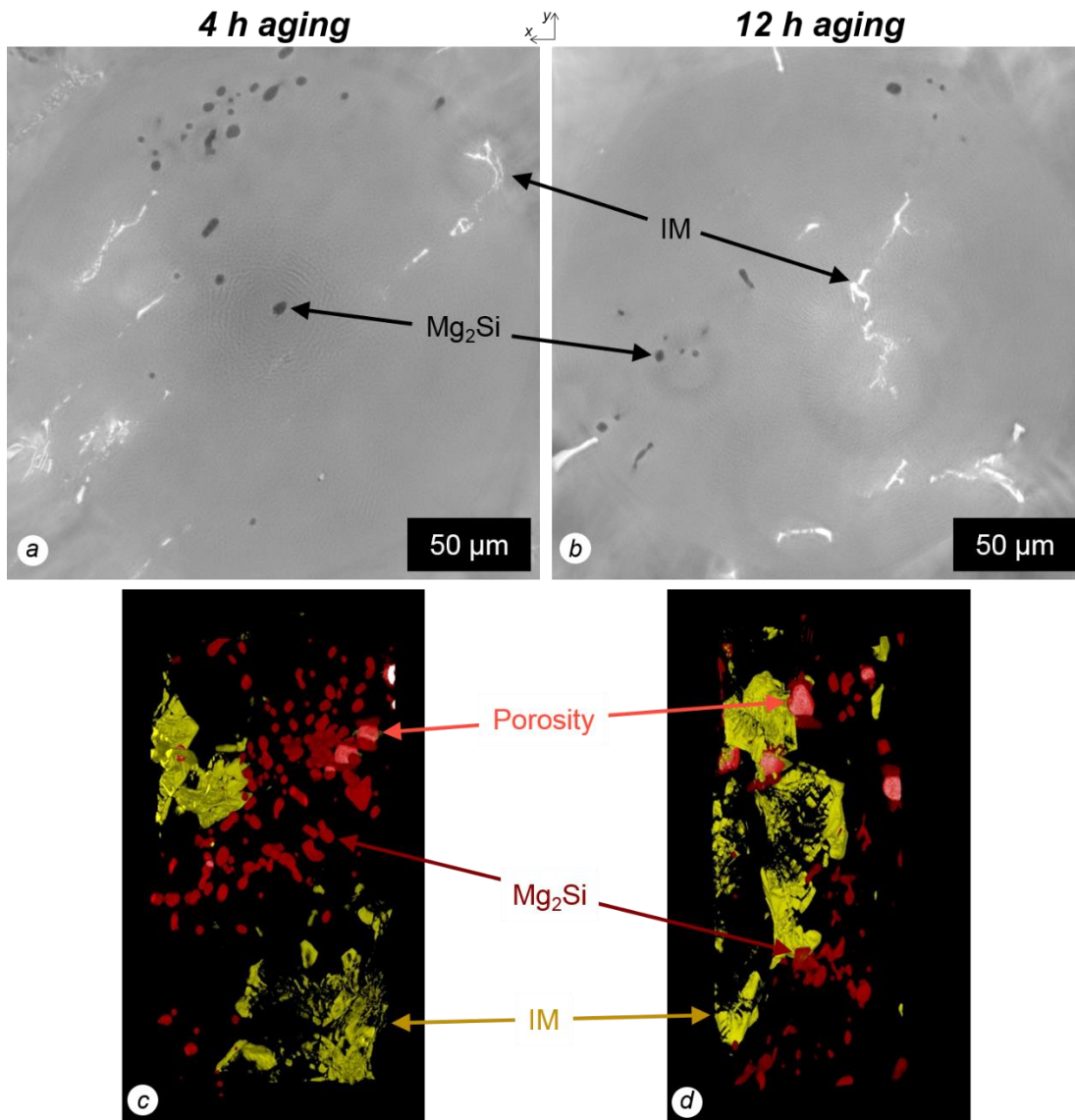


Figure 3 – 2D and 3D ($80 \times 80 \times 200 \mu\text{m}^3$) visualisations of IM particles, porosity and clusters of Mg_2Si using nano-laminography scan (undamaged materials) after 4 and 12 h aging

3.1.2. Hardening precipitation

Macroscopic mechanical behavior changes are necessarily due to microstructural evolutions. Since no changes at the micrometer scale were observed in the previous paragraph, investigations must be conducted at the nanoscale. In order to highlight nanoscopic trends induced by aging time according to the precipitation sequence described above, the application of atom probe tomography (APT) to study our materials is suited.

A comparison is shown in Figure 5 between an APT-tip aged 4 h and a tip aged 12 h. The blue points are the aluminum ions, and the red surfaces represent the isoconcentration surfaces where the magnesium concentration exceeds 3%. These areas also correspond to silicon concentrations greater than 3%. They therefore represent the magnesium and silicon precipitates induced by the precipitation sequence [18–21].

It is shown that hardening is ensured by the formation of β'' precipitates during aging. Figure 5 shows that there is an increase in the size and density of this hardening nanoprecipitation with the aging time, as described by Zandbergen [35]. A third specimen (112 million evaporated ions, 464 nm long) is shown in Appendix A and demonstrates the intense presence of this hardening precipitation on the 12 h aged material. The obtained precipitates form clusters and needles.

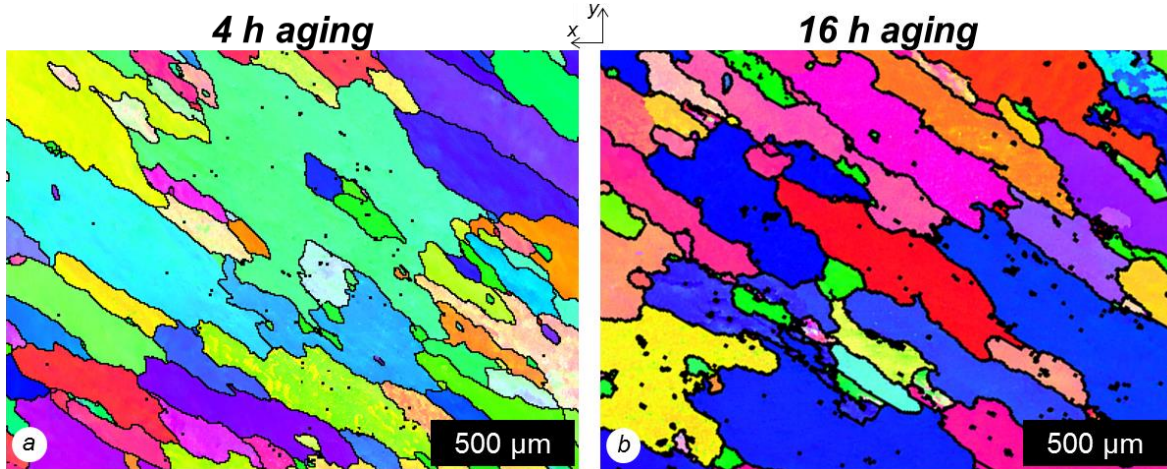


Figure 4 – EBSD map of the typical grain distribution in the XY plane after 4 and 16 h aging. Different colors indicate different grains.

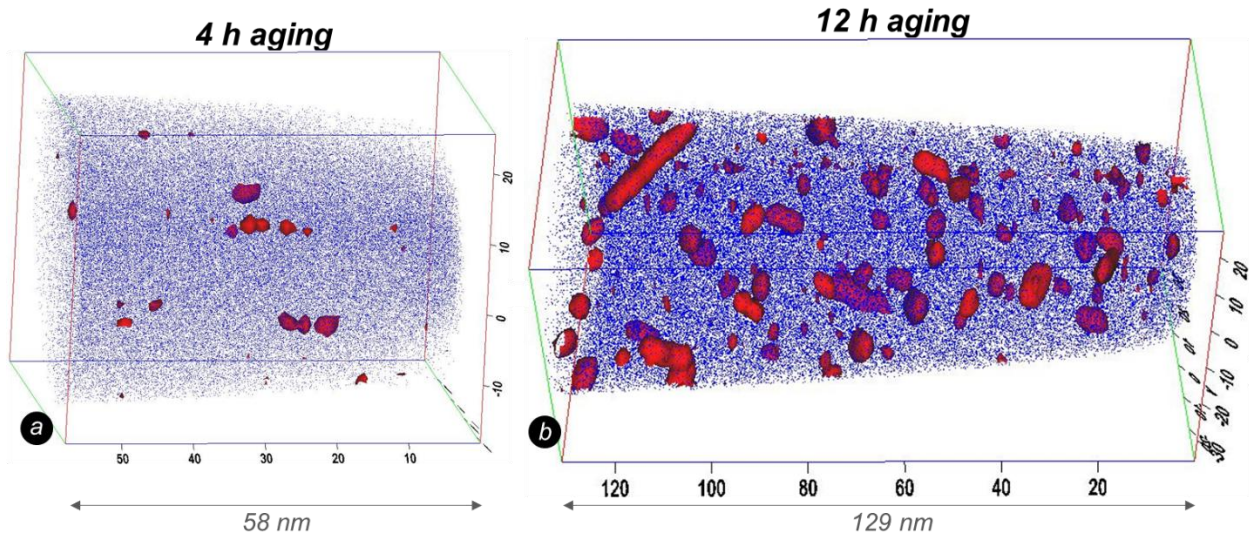


Figure 5 - Comparison of two APT tips after 4 h (2.1 million ions analyzed) and 12 h aging (8 million). The red isosurfaces represent areas of high concentration of Mg (> 3%) in the aluminum matrix represented in blue.

The main conclusions from this part are the following: on the undamaged material and at the microstructural level, the observed macroscopic mechanical evolutions are related only to the higher amount of nanoprecipitation and to the larger precipitate size, and therefore to the structural hardening.

3.2. Fracture mechanisms

The aim of this part is to identify the damage micromechanisms governing the fracture of the 6061 aluminum alloy as a function of aging time and at high levels of stress and stress triaxiality, firstly *post mortem* in two dimensions through fractographs, secondly through X-ray laminography in order to study the damage micromechanisms in three dimensions in samples containing stopped cracks. The study is performed in light

of results of the literature [1–3] and to acquire the physical basis to build a micromechanical model to reproduce the effect of aging on toughness.

3.2.1. Fractography

The fractographs of the 4 h aged and 16 h aged materials (Figure 6) show typical ductile fracture surfaces. Fractographs *a* and *b* in Figure 6 observed with secondary electrons show that dimples completely cover the fracture surfaces and ductile failure micromechanisms are identifiable. It has been founded that many dimples contain at their bottom one or several broken or unbroken particles, identified as mostly broken Mg_2Si by EDS analysis. The characteristic dimple size does not substantially evolve with aging time. The void growth to coalescence is visible.

To identify the amount of iron rich intermetallic particles, which are hard to observe with secondary electrons, the same areas were observed in backscattered electron mode. For the 16 h aged material more intermetallic particles are found on the fracture surface. Some huge clusters may have diameters around 200 μm which correspond to the previously measured cluster size. The area fraction is not very easy to determine due to the surface roughness that also contributes to contrast changes. However, the same procedure was applied to both heat treatment conditions and a factor of 2 to 3 in area fraction difference is always found between the 4 h aged material and the 16 h aged material: the area fraction of intermetallic particles was estimated as 1.7 % ± 0.2 for the 4 h aged material and 4.6 % ± 0.6 for the 16 h aged material. Note that the intermetallic particle area fraction of the 4 h aged material is similar to the area fraction of intermetallic particles found for random cut and polished sections of the undamaged material which seems to indicate that they do not play a major role for the rupture of the 4 h aged material.

Void coalescence by internal necking after nucleation is the main mechanism, and only on some small areas the coalescence by void-sheeting, as described by Garrison and Moody [36], can be observed. Therefore, it may be concluded that coarse particles (Mg_2Si and intermetallic phases) control failure.

The dimple size seems similar for both materials but maybe for different reasons. For the 4 h aged material voids nucleate on Mg_2Si particles as well as on small parts of iron rich intermetallic particle clusters and lead to substantial void growth, whereas for the 16 h aged material the area of nucleated particles is higher. This may lead to a similar dimple size but it may involve less void growth for the 16h aged material.

The intermetallic phases may play a role at later damage stages. As shown by Shen et al. [10], large Mg_2Si inclusions crack for very low plastic strain levels and defects are nucleated at large (Fe,Si)-rich inclusions with increasing plastic deformation.

Figure 6 shows no difference in damage mechanism for the various aging treatments, despite the different crack propagation resistance. It therefore seems that the increasingly low observed tearing moduli result from an acceleration of the ductile failure, and not from a modification of the fracture mechanisms. We will investigate further these fracture mechanisms in the next parts.

3.2.2. Investigations after interrupted toughness tests

After interrupted fracture toughness tests, slices with a thickness of 1.5 mm were machined from CT specimens in two different directions: in the plane of crack propagation and in a transverse plane (Figure 7 *d*).

Laminography

Classical ductile fracture (Figure 7) and a very rough crack surface are observed for these 2D section of 3D laminography data normal to the crack propagation direction. The three different aged samples show no significant difference in fracture micromechanisms. A recomposition of a section through the entire sample width obtained by stitching 23 scans is given in Appendix B, after 12 h aging.

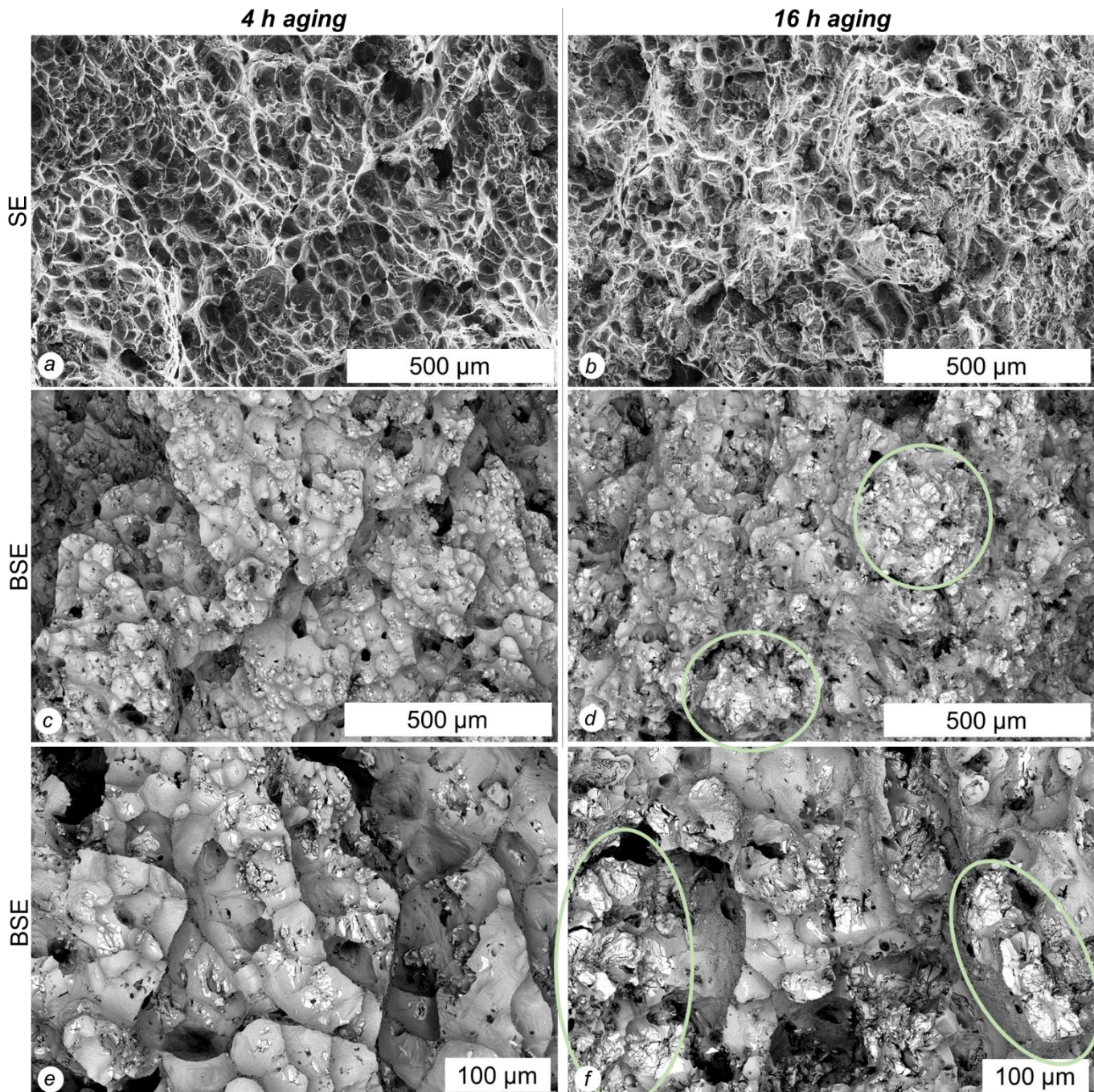


Figure 6 – Comparison of fracture surfaces (fractography) after fracture toughness tests using two CT specimens after 4 and 16 h aging. The figures a/c and b/d are taken in the same zone using Secondary Electron (SE) and BackScattered Electron (BSE) detectors. The figures e and f are taken by BSE in another zone. The green circles show the IMs clusters.

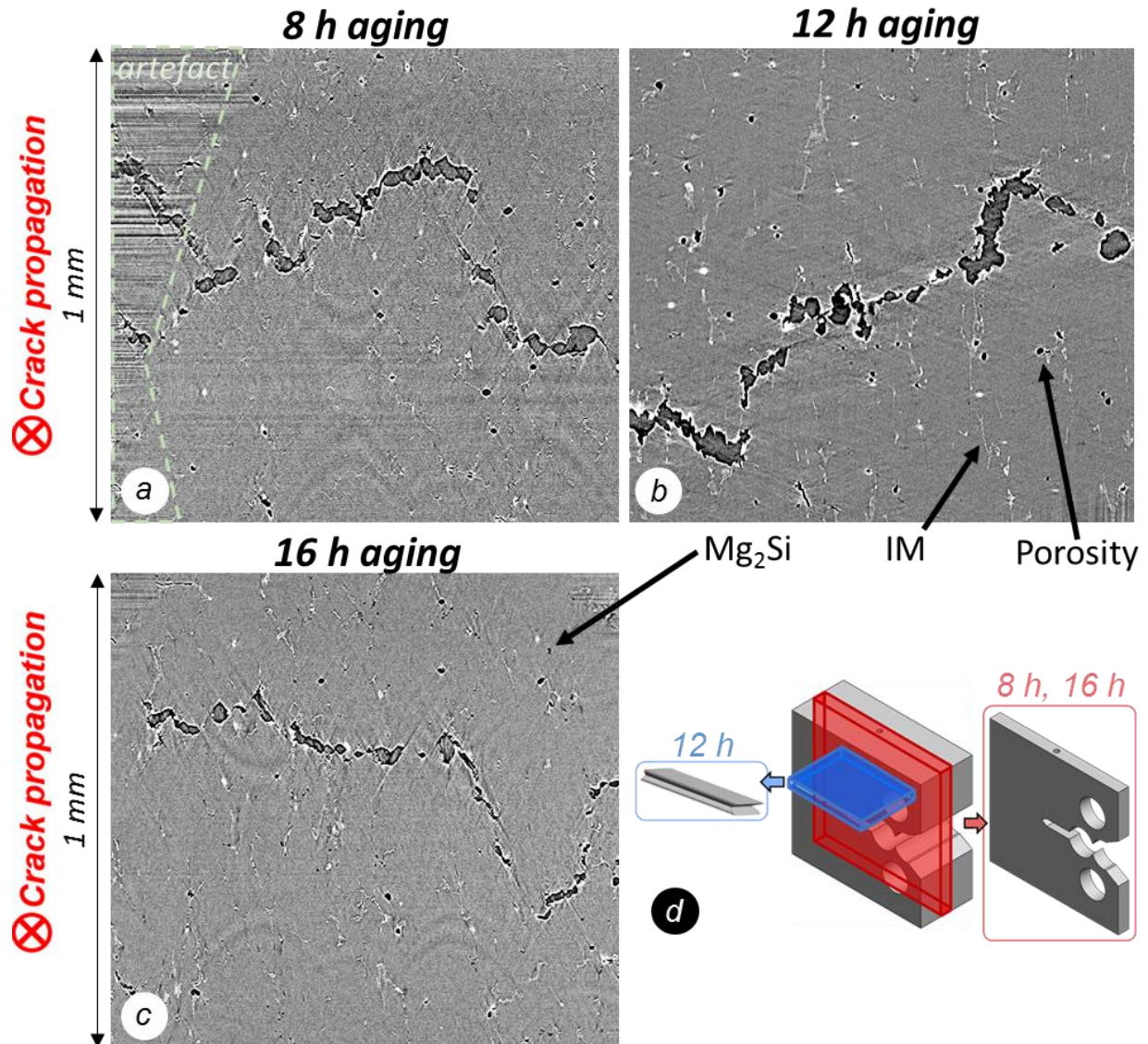


Figure 7 – Comparison of fracture mechanisms in CT specimens observed by SRCL, 300 μm behind the crack tip. Specimen after 12 h aging were machined in accordance with the blue sample in the d) drawing, specimen after 8 and 16 h in accordance with the red sample. Figure a) contains projection truncation artefacts.

The void coalescence by internal necking is the main mechanism governing fracture, but in some small areas the coalescence by void-sheeting (Figure 8) can be observed, as also seen on fractographs. In order to visualize the fracture profile and the crack tip damage, a volume of $520 \times 1664 \times 260 \mu\text{m}^3$ around the crack tip was selected for a 3D visualization (Figure 9). A heterogeneous presence of large clusters of porosity at the crack tip is visible and the rupture is classically ductile. The amount of observed damage seems rather high, with many cavities (from 5 to 20 μm diameter), among which some have coalesced, without connection to the crack yet. Scans realized on the 16 h aged material are very centered at the crack tip (Figure 10). Artefacts called “rings” are due to a defect in the optical path (imperfections on the scintillator, defective pixel on the detector...). These scans allow us to visualize the damage mechanisms downstream of the crack, in particular the nucleation on IMs and the void growth. This highlights that nucleation on IM particles may well play a role on fracture here. In particular, their oblate shape makes them more detrimental than particles with globular shape. When the IM particles fracture, they largely contribute to the fracture

surface despite their small volume. The high reached levels of stress at the crack tip of this hardest material aging condition may additionally have contributed to their brittle fracture by reaching a critical principal stress. These damage features resemble the large iron rich intermetallic clusters of Figure 6 also found on the fracture surface of the 16h aged material. It highlights the brittle nature of the particles and the effect of stress level on damage nucleation.

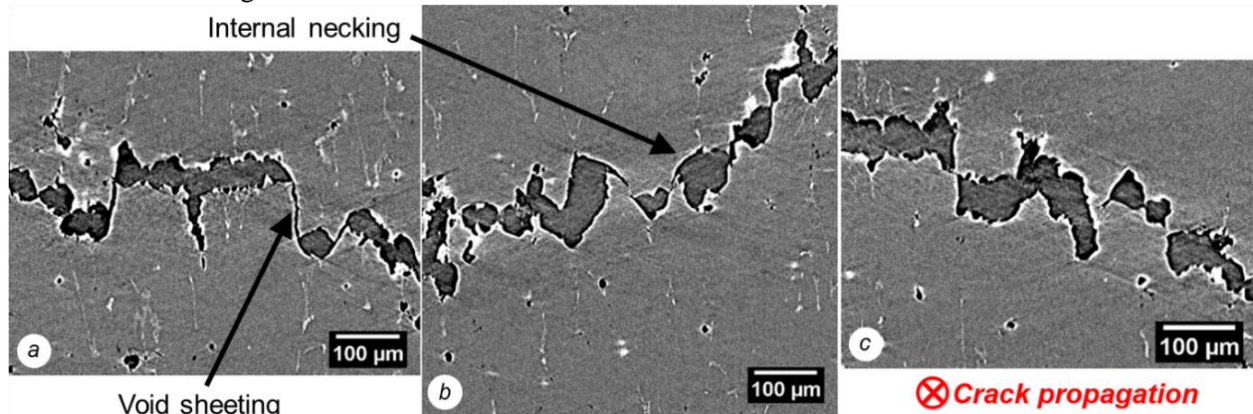


Figure 8 - Void coalescence by internal necking and void-sheeting on slice of CT sample (12h aging) observed with SRCL

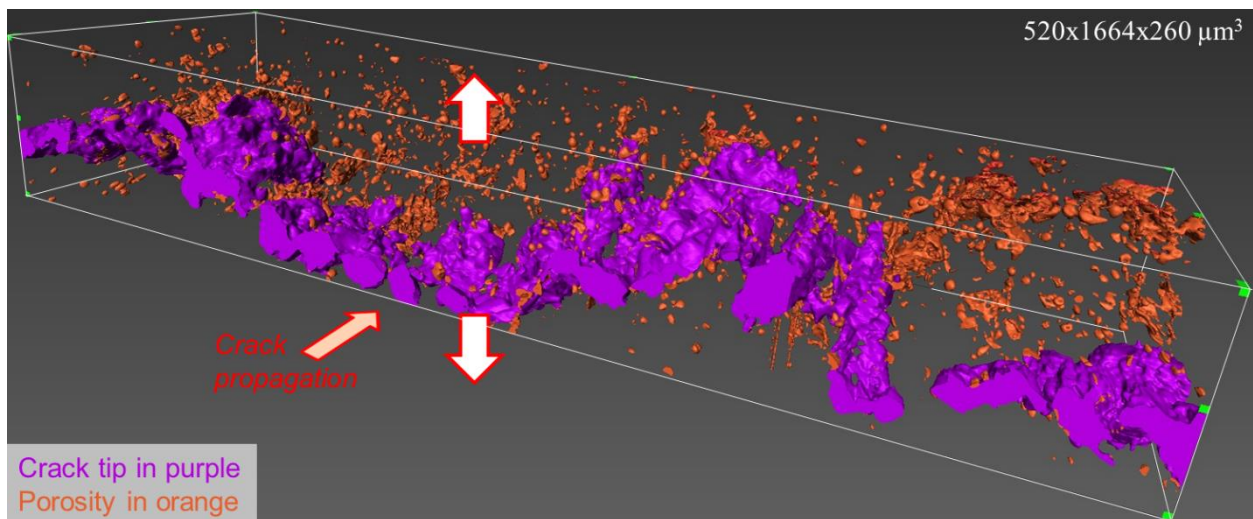


Figure 9 – 3D visualisation of the crack tip and of porosity for a CT sample (12 h aging)

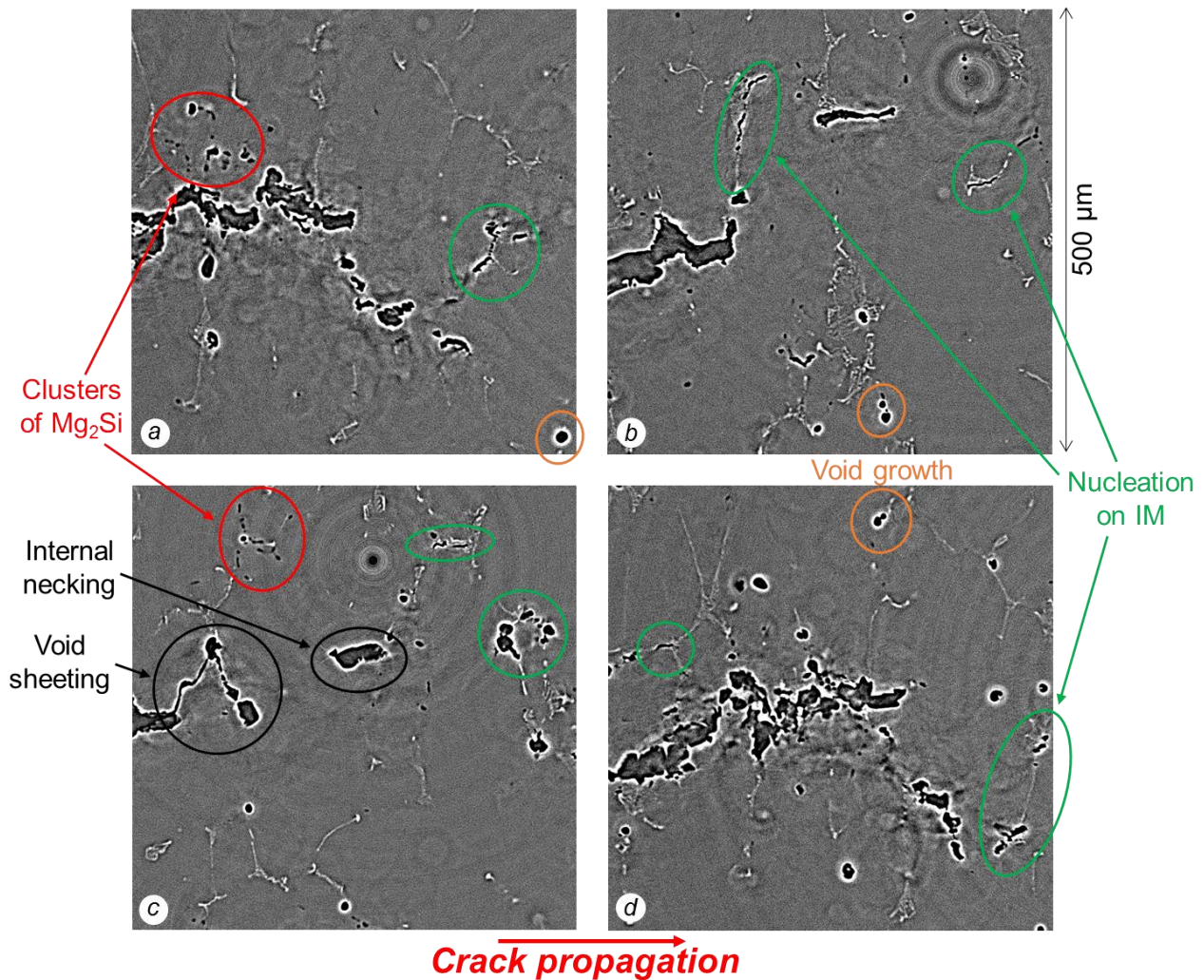


Figure 10 - Damage mechanisms at the crack tip of a CT sample of 16 h aged material shown by different 2D sections along the crack front of 3D laminography data of an interrupted crack

EBSD examination at crack tip

As explained in section 1, the studies of Dumont et al. [1–3] highlight the important role of the fracture mode (inter- or transgranular). It seems essential to further investigate this aspect in this section, where the crack propagation is investigated via EBSD analysis on polished and etched samples containing interrupted cracks. These EBSD analyses are performed at the crack tip to visualize the grain distribution around the crack (Figure 11). The damage is dominated by nucleation on coarse particles, and the cracks follow these particles, located within the grains. The fracture mode is indeed mainly transgranular (estimated around 70–75 % of the surface for the shown sections), which can be explained by the previously observed random distribution of coarse particles that did not particularly involve grain boundaries (Figure 2). An intergranular fracture (around 25–30 %) exists here only around the small grains, which are strongly misoriented and contain particles at the grain boundaries. This is in contradiction with what Shen et al. [10,33] had shown: the particles appeared to be localized preferentially at the grain boundaries. This also stands in contradiction with the results of Dumont et al. [1–3] who found an increase of intergranular failure with aging. This may be due to the fact that a different series of Al-alloys is studied here and to the fact that our heat treatment does not pass the peak aged condition.

Scanning Electron Microscopy as well as 3D X-ray tomography show that the characteristic damage mechanisms do not depend on aging time: large Mg_2Si inclusions crack for very low plastic strain and defect are nucleated at large (Fe,Si)-rich inclusions with increasing plastic deformation, and the rupture is mostly transgranular.

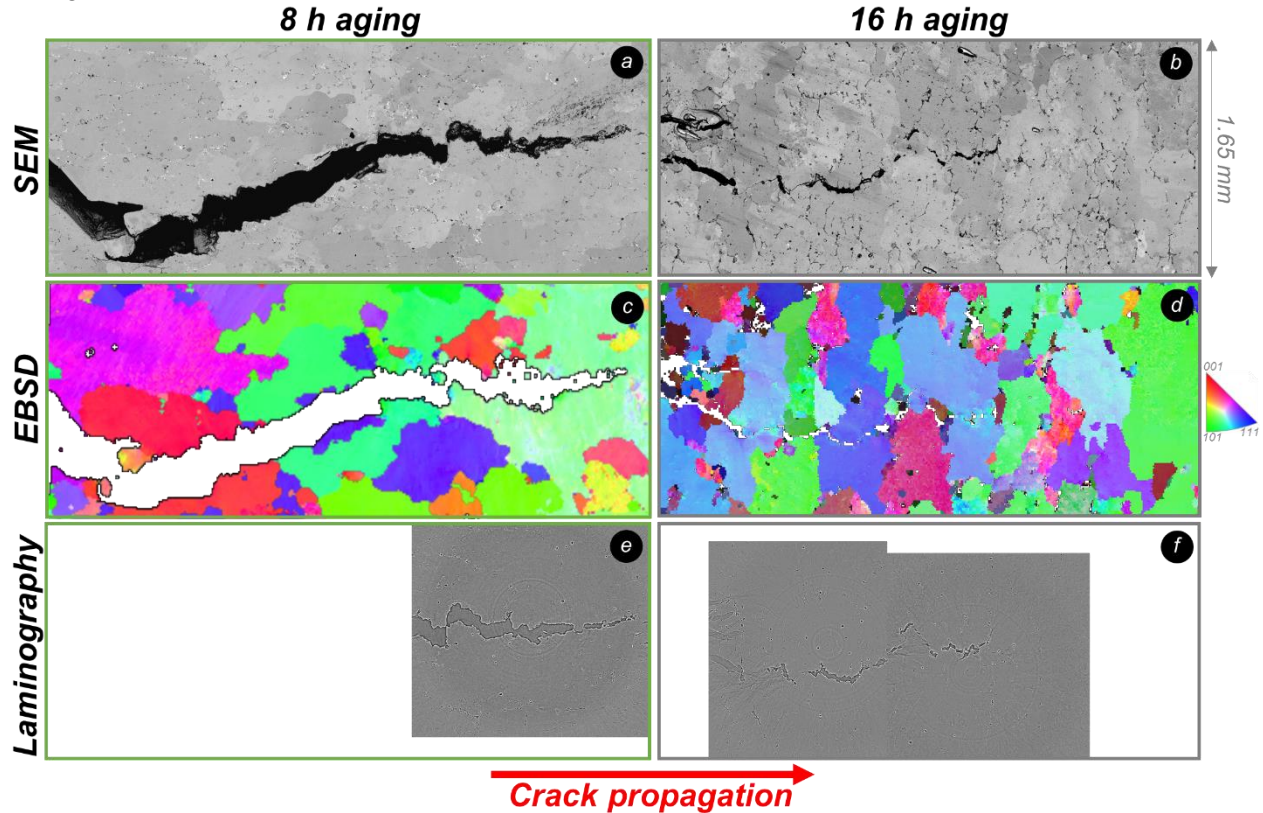


Figure 11 - Correlative investigations using SEM (a/b), EBSD (c/d) and laminography (e/f) of two slices of CT specimens after interrupted toughness tests (8 h aging for a/c/e, 16 h aging for b/d/f)

4. Simulation of toughness

The aim of the section is to simulate the decrease in both crack initiation toughness and tearing modulus with aging time. As observed earlier, damage mechanisms do not change with increasing aging time and they are typically ductile. In particular, the volume fraction of particles at the origin of damage (Mg_2Si and IMF) remains constant. The only effect of aging is the increase in yield stress and ultimate tensile strength, and the decrease in hardening modulus due to the precipitation of nano-sized strengthening particles. The model proposed below is based on these observations.

4.1. Model for ductile tearing

To derive the model, the plastic behavior of each material is assumed to obey von Mises plasticity with isotropic hardening. Hardening is represented by a Voce [37] law fitted for each heat treatment based on tensile tests performed on smooth specimens [11] as:

$$\sigma = \sigma_S + (\sigma_e - \sigma_S)e^{-b\varepsilon_p} \quad \text{Eq. 1}$$

The fit is performed up to the necking strain (ε_u). It will be shown below that failure strains are close to ε_u , so that the fit is used without extrapolation. The four sets of parameters of the Voce law are gathered in Table 3.

		σ_s	σ_e	b
		MPa	MPa	
Aging (h)	4	322.36	154.00	12.12
	8	344.60	199.33	12.72
	12	352.09	237.33	14.27
	16	354.51	255.00	17.34

Table 3 – Voce hardening law parameters for all heat treatments

Damage development is accounted for by the Gurson-Tvergaard-Needleman (GTN) model [38] which is able to represent ductile failure in metals resulting from an overlapping sequence of nucleation, growth and coalescence of small internal voids leading to macroscopic fracture [39,40]. The model is a semi-empirical extension of the micromechanical model initially proposed by Gurson [41]. Note that numerous extensions of the model have been proposed which are reviewed e.g. in [42–45]. The GTN model is based on the definition of a yield surface expressed as:

$$\Phi = \frac{\sigma_{eq}^2}{R^2} + 2q_1 f_* \cosh\left(\frac{1}{2} q_2 \frac{\sigma_{kk}}{R}\right) - 1 - q_1^2 f_*^2 \quad \text{Eq. 2}$$

where σ_{eq} is the von Mises stress, σ_{kk} the trace of the stress tensor, R the flow stress of the matrix (undamaged material), q_1 and q_2 model parameters describing void growth. f_* (which may be interpreted as an effective porosity) is a function of the actual total porosity f_t . It was introduced to model coalescence in a rather simple but efficient way. More sophisticated models for coalescence have been proposed based on the seminal work of Thomason [46,47] as in [48–50]. Following the GTN model, it is assumed that when a critical porosity f_c is reached, damage increase is faster due to coalescence. To represent this trend, the f_* function is written as follows (where f_R is the fracture porosity):

$$f_* = \begin{cases} f_t & \text{if } f_t \leq f_c \\ f_c + \left(\frac{1}{q_1} - f_c\right) \frac{f_t - f_c}{f_R - f_c} & \text{otherwise} \end{cases} \quad \text{Eq. 3}$$

The total porosity f_t is expressed as the sum of the porosities due to growth (f_g) and due to nucleation (f_n):

$$f_t = f_g + f_n \quad \text{Eq. 4}$$

It is then necessary to define the evolution laws for the different material variables. The plastic strain rate tensor is expressed as:

$$\dot{\underline{\varepsilon}}_p = \lambda \frac{\partial \Phi}{\partial \underline{\sigma}} \quad \text{Eq. 5}$$

where the plastic multiplier λ is obtained writing the consistency condition. The isotropic hardening variable p is obtained writing the equality between macroscopic and microscopic dissipation:

$$\dot{\underline{\varepsilon}}_p : \underline{\sigma} = (1 - f_t) \dot{p} R \quad \text{Eq. 6}$$

The evolution of the growth porosity f_g is obtained writing mass conservation so that:

$$\dot{f}_g = (1 - f_t) \text{tr} \dot{\underline{\varepsilon}}_p \quad \text{Eq. 7}$$

Due to the high coarse particles content, void nucleation is an important damage mechanism in the studied material [10] as in many aluminum alloys [7,34,51,52]. In the literature, strain and stress controlled nucleation kinetics have been proposed [7,42,53] but most models use strain controlled nucleation. In that case, the nucleation rate (\dot{f}_n) may be expressed in a generic way as:

$$\dot{f}_n = A_n(\dots)\dot{p} \quad \text{Eq. 8}$$

where A_n is a material parameter which may depend on material state variables. In most cases, A_n only depends on plastic strain p . For instance Chu et Needleman [12] introduced a Gaussian function, using three material parameters (f_N is the volume fraction of inclusions at which damage can be nucleated, ε_N the strain for which 50% of the inclusions are broken, s_N the standard deviation on the nucleation strain):

$$A_n = \frac{f_N}{s_N\sqrt{2\pi}} \exp\left(-\frac{1}{2}\left(\frac{p - \varepsilon_N}{s_N}\right)^2\right) \quad \text{Eq. 9}$$

But many other forms are used [54–56]. More complex formulations may be used ; for example Ueda et al. [30] introduced two strain controlled nucleation kinetics to distinguish two populations of differently sized precipitates. Most models for stress controlled nucleation use the maximum over loading history of the main principal stress to obtain the volume fraction of broken/debonded inclusions. The effect of stress state may also be described using a strain controlled nucleation law for which A_n is expressed as a function of stress state. For instance the nucleation rate was considered as depending on stress triaxiality in [13].

In this study, the full model was implemented in the Z-Set Finite Element software (<http://www.zset-software.com/>). Simulations were carried out using 3D linear hexahedra using selective integration to avoid spurious pressure oscillations [57] (8 Gauss points per element). Standard boundary conditions are used so as to limit the simulation to ¼ of the CT specimens (Figure 12). A fixed mesh size h is used within the region of crack propagation due to the softening character of the constitutive equations. Elements are removed from the simulations once 4 Gauss points have reached a state where $f_t = f_R$ [58].

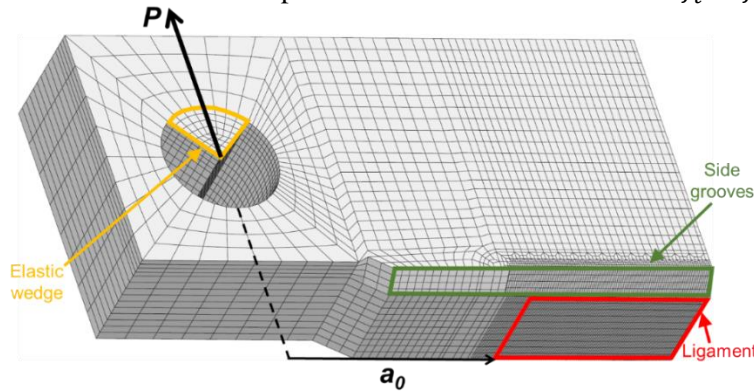


Figure 12 – Mesh of a quarter of a side grooved CT specimen

4.2. Stress-based nucleation criterion

In this study, it will be tried further to reproduce the experimental results using nucleation kinetics which indirectly depend on aging time. As aging affects yielding and hardening but leaves particles state and damage mechanisms unchanged, it is assumed that the increasing stress level will favor nucleation at lower levels of strain as aging time increases. It is therefore proposed here to use a single stress- and strain-based nucleation rate $A_n = A_n(p, \sigma_I)$ where σ_I is the maximum principal stress.

As demonstrated in the previous results section, simulations without nucleation, or using a Chu and Needleman nucleation term, do not capture the effect of aging on toughness. A stress-based nucleation criterion is thus proposed (Figure 13):

$$A_n(p, \sigma_I) = \begin{cases} 0 & \text{if } \sigma_I \leq \sigma_S \text{ or } p \leq p_S \text{ or } f_n = f_N \\ A_{n0} \left(\frac{\sigma_I}{\sigma_S} - 1 \right)^2 & \text{otherwise} \end{cases} \quad \text{Eq. 10}$$

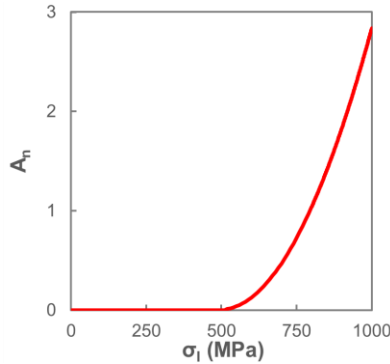


Figure 13 – Stress dependance of the nucleation model

p_S and σ_S are respectively the strain and the stress below which nucleation cannot be active. f_N is the volume fraction of inclusions at which damage can be nucleated.

4.3. Model parameter adjustment

The three-dimensional qualitative and quantitative study proposed by Shen et al. [10] is used to identify the GTN micromechanical damage model. The coarse Mg_2Si particles start to be damaged in the very early loading stage. As a consequence, these particles are considered to be pre-existing voids. Their volume is therefore considered as the initial porosity f_0 in the simulations. Cavities nucleating on iron-rich intermetallics are taken into account in the void nucleation parameters. The volume fraction of iron-rich intermetallics obtained by SEM analysis is considered to be the maximum value (f_N) that can be nucleated. The remaining parameters (q_1 , A_n) are adjusted so as to match the experimental results. q_2 is assumed to be equal to 1 as seen in the literature [38].

For the Chu and Needleman nucleation model, the values $\varepsilon_N = s_N = 10\%$ determined by Shen et al. [10] via in situ synchrotron laminography investigations are used here.

In the stress-based nucleation model, p_S corresponds to the plastic strain below which nucleation does not occur. A_{n0} and σ_S are adjusted to fit the experimental data. Finally the nucleation function is expressed in such a way that the nucleated porosity never exceeds f_N . The parameters (Table 4) are automatically tuned using an optimization software (Levenberg–Marquardt algorithm). In order to reduce computation time, a 2D plane strain model of the CT specimens was first used. It was checked that these simulations remain very close to the full 3D simulations. In the following part of the manuscript, only 3D results are shown.

4.4. Results and discussion of the simulations

Figure 14 shows the load – CMOD (Crack Mouth Opening Displacement) curves corresponding to the experimental tests (lines with markers) and three simulations for each aging time: the first (dashed lines) uses an elastoplastic law without damage, the second (dotted lines) uses GTN law without nucleation, and the third (points) uses GTN law with a classical Chu and Needleman nucleation. It can be seen that the

predictions for both the simulation without nucleation and for the Chu and Needleman nucleation criterion are poor.

		Pre-existing voids and void nucleation							Void growth		Void coalescence		Element size
		f_0	f_N	Chu Need. nucl.		Stress-based nucl.			q_1	q_2	f_c	f_R	h
				ε_N	S_N	σ_S	p_S	A_{n0}					
		%	%	%	%	MPa	%			%	%	μm	
Aging (h)	4	0.35	2.15	10	10	500	3.21	2.92	2	1	4.0	5.6	100
	8												
	12												
	16												

Table 4 – Single set of damage parameters for all heat treatments

For the simulations without nucleation, only the initial porosity and Mg_2Si particles are accounted for and considered as initial porosity. For the high toughness condition (4 h aging) a good agreement with the experimental curves is obtained. With these parameters the load-CMOD curves are overpredicted for all other heat treatment conditions. Indeed, as shown in Figure 10, nucleation on iron-rich particles may also play a role for nucleation and toughness reduction but is not accounted for in the simulations.

If the nucleation is accounted for in a classical way, using the strain based nucleation criterion by Chu et Needleman [12] and a single set of the parameters identified by Shen et al. [10], the pointed curves in Figure 14 are obtained. For the material that was aged for 12 h, the simulation corresponds well to the experiments. This is consistent with the fact that the parameters by Shen et al. [10] have been fitted for an AA6061 alloy in T6 condition which corresponds to 12 h aging.

The load-CMOD curve for 16 h aging is slightly overpredicted whereas for the 4 and 8 h aging conditions the curves are strongly underpredicted. This result is expected since the nucleation is based on strain only. Due to higher ductility of the 4 h aged condition, the predictive capabilities of this nucleation criterion are poor for 4 h aged toughness behavior as the strain at which failure occurs experimentally is higher for this material. The used Chu and Needleman (C-N) parameters [10] are too severe for this condition. For a given CMOD but various hardening laws the local stress triaxiality is hardly changed, as it is a stress ratio, and plastic strain, which is driving nucleation, is also almost unchanged. Consequently, using a given set of parameters of the C-N law for all heat treatment condition leads to an underprediction of toughness for the short aging times and to an overprediction of toughness for long aging times. For each aging condition a new set of parameters of the C-N model would need to be fitted to reproduce the toughness curves for all heat treatment conditions. This would lead to 12 parameters in our case. Using our proposed model only 3 parameters need to be adjusted.

Thus a different modelling approach, e.g. in the form of a stress-based nucleation criterion, is needed to capture the effects of material strengthening on toughness. When fitting the parameters of the stress-based nucleation function presented in section 4.2 using the toughness data, a very good agreement between experiments and simulation (Figure 15) is achieved with a unique set of damage parameters for all heat treatment conditions. Only the hardening parameters are different for each heat treatment condition.

This good fit highlights that the physics of the damage process are better captured using this criterion. Indeed, the damage mechanisms have been identified as void growth after nucleation on the coarse particles. The iron-rich particles fail at later stages of strain. As the failure of intermetallic particles (and their debonding) is a cleavage process, and which is driven by critical principal stress [59,60], this principal stress needs to be accounted for in the nucleation term. The formulation of an adequate condition for void

nucleation by interface fracture is a difficult problem [61]. This explains why many researchers attempted to solve this problem through “phenomenological” models (see Chu and Needleman [12]; Tvergaard [42]). In finite element simulations, stress-based nucleation criteria often introduce numerical instabilities, which also explains the popularity of the strain driven Chu and Needleman [12] nucleation term. The stress-based nucleation term suggested here is also based on strain which makes it numerically robust. As the nucleation curve is smooth there are no convergence issues. Another advantage is that after the stress maximum achieved in each element during tearing the nucleation still continues but to a lesser extent.

To better highlight the role of stress on damage, Figure 16 shows the evolution of the maximum principal stress and the total porosity f_t (composed of the porosities due to growth f_g and due to nucleation f_n) as a function of the plastic strain. The maximum principal stress increases sharply with aging time. It can be seen that the nucleation contribution is much smaller than the growth contribution (and that it is even reduced to zero after 4 h aging). However, this contribution, although small, has a significant effect on the ductile tear resistance. The distribution of these two contributions is consistent with the experimental observations. Indeed, on the fractographs, broken Mg_2Si are identifiable in the bottom of the dimples; these particles have been considered as initial porosity and play a preponderant role in growth. In addition, the fact that nucleation on IMs plays a more important role at high aging times (Figure 16 c) is qualitatively in agreement with the BSE fractographs showing more iron rich particles for 16 h aged material (Figure 7 d and f). Laminography makes it possible to observe this secondary role of IM, which are sites of preferential nucleation (Figure 10).

In the present work the increasing part of the aging-strength curve has been assessed in terms of strength toughness relationships. In the literature it has been found that after peak aging, toughness may continue to increase above the peak-aged value [1–3,62]. This effect could be captured with the present modelling approach, as the flow stress diminishes after peak aging. Often the toughness after peak aging does not return to the same level as for the same yield stress level in under-aged condition. If the same damage mechanisms are at play for these different conditions (i.e. no additional intergranular failure) this behavior could be captured by the present approach. The hardening behavior of the overaged condition thus needs to be assessed. This hardening is often seen reduced in the over-aged condition and might also lead to a toughness reduction in the simulation as the process zone would decrease.

As a matter of fact the present study shows that the model by Hahn and Rosenfield [63], in which toughness is proportional to the square root of the materials’ yield stress, is not suited to predict the toughness of Al-alloys as the detrimental effect of stress level leading to increased damage nucleation is not accounted for.

Experimentally, it would be difficult to quantify or even to observe the evolution of the nucleation kinetics as a function of aging time. One possible solution would be to perform ex-situ interrupted tests using specimens or configurations with comparable triaxiality. Indeed, in-situ tensile tests (even on notched specimen) do not make it possible to reach such a high triaxiality state as in CT samples, and therefore do not make it possible to reach maximum principal stress values σ_I which could be large enough to activate the nucleation model ($\sigma_I > \sigma_S$). In addition, nucleation is initiated at very small scales, especially since the IMs play a secondary role in relation to the Mg_2Si particles. Therefore, extremely fine analyses would be required to quantify such slight evolutions as illustrated in Figure 16 c (as mentioned before, even slight microstructural evolution can cause macroscopically significant deterioration of toughness). Furthermore the material exhibits heterogeneity as the grain size can be in the order of hundreds of micrometers. As a result, statistical relevance needs to be considered in further studies.

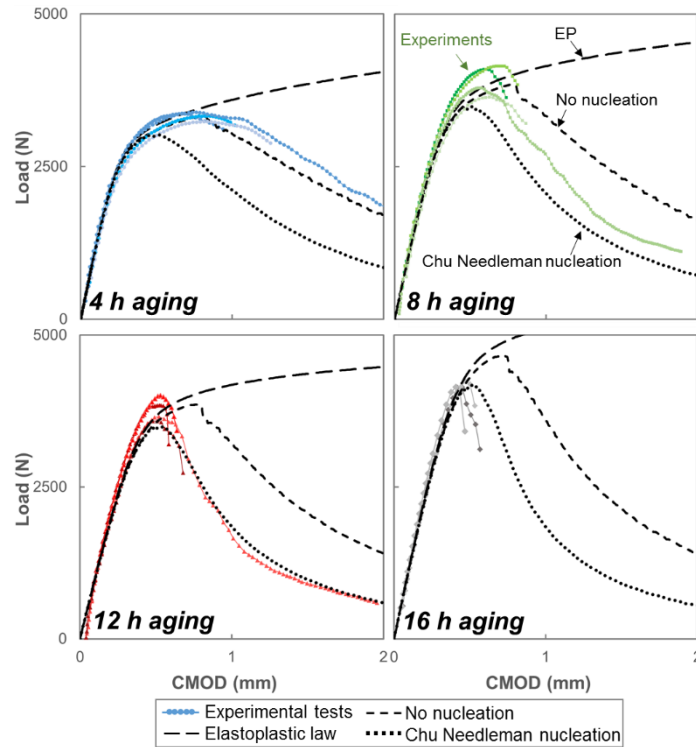


Figure 14 – Experiments (lines with markers) and simulations of toughness tests. All the GTN damage parameters are the same, only the Voce elastoplastic law differs between each aging time: dashed lines correspond to the simulations using elastoplastic law, dotted lines to the simulations without nucleation, points to the simulations using Chu and Needleman nucleation.

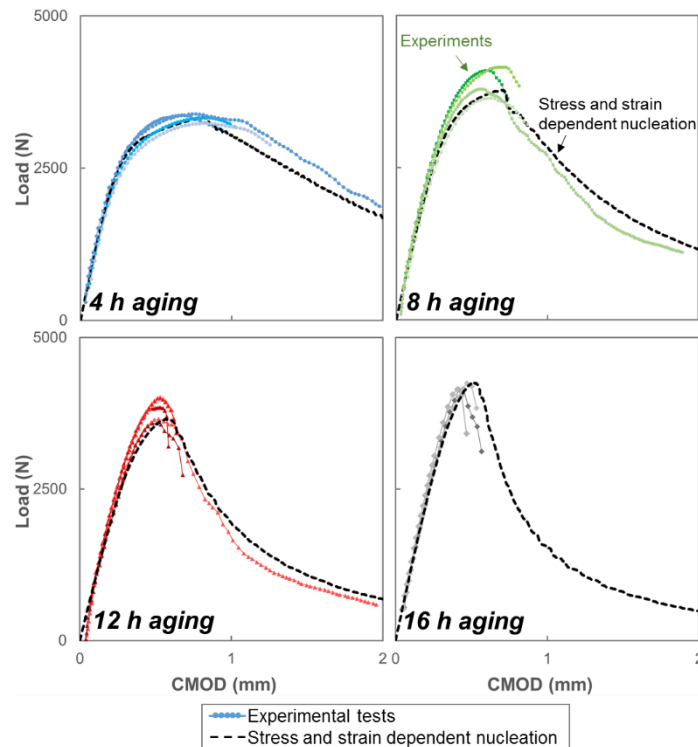


Figure 15 – Experiments and simulations of toughness tests with the stress-strain-based nucleation law. All the GTN damage parameters are the same, only the Voce elastoplastic law differs between each aging time.

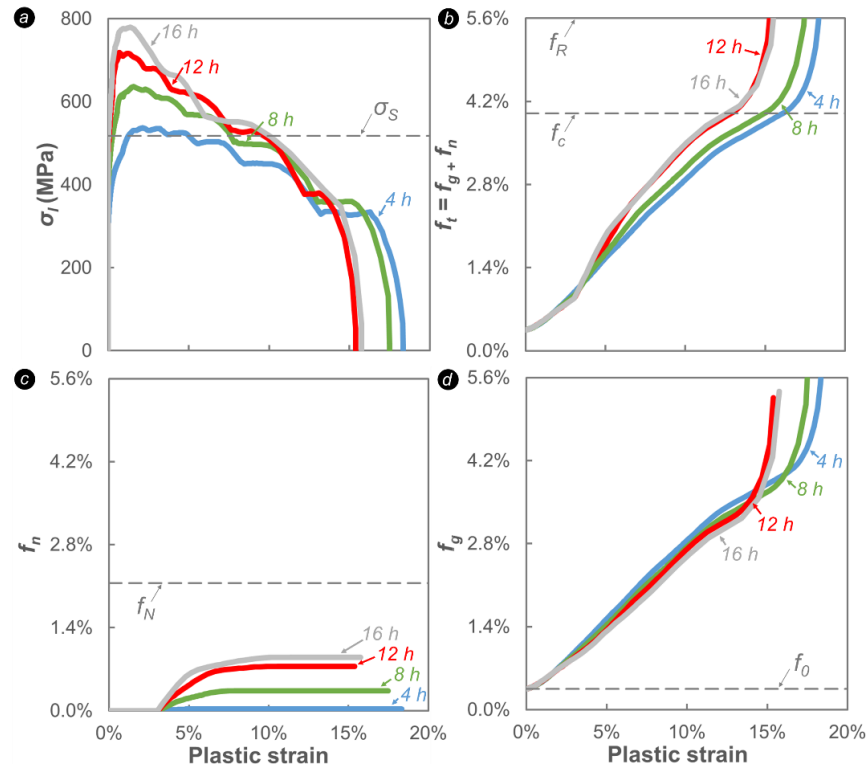


Figure 16 – Evolutions of the maximum principal stress and porosity fractions due to nucleation and growth during simulations for the four aging times

5. Conclusions

Aging causes a decrease in toughness, including of the tearing modulus. This deterioration is accompanied by an increase in the tensile properties, and thus also by an increase in the stress levels reached in the material.

Damage nucleation and growth originate from coarse particles, in the form of micrometer sized Mg_2Si and iron-rich intermetallic particles for all heat treatment conditions. The characteristic fracture mechanisms, which are governed by these phenomena, do not evolve with aging time: indeed fractography as well as laminography and EBSD investigations of stopped cracks, have shown that the fracture mode is typically ductile (even for the lowest tearing resistance) and mainly transgranular. However, it has been identified through quantitative fractography of the 4 h aged and 16 h aged CT samples, that the area fraction of iron rich intermetallic particles is two to three times higher for the longest aging time. The size of the broken clusters for the longest aging time is also bigger and similar to the full particle cluster size measured on cut sections. It can be concluded that at the microstructural level, the mechanical evolutions are only accompanied by a modification of the nanoprecipitation (which was confirmed by APT analyses), responsible for the structural hardening in the Al-matrix. This hardening of the matrix promotes damage nucleation on coarse particles as it can be considered to be a cleavage-like process that allows to fracture the entire iron rich intermetallic clusters for the longest aging time and highest associated stress levels.

It is therefore proposed to model this toughness deterioration by modifying only the macroscopic material hardening and using a *single* damage nucleation growth and coalescence law. Nucleation plays a predominant role here, and the modeling of the strain-based nucleation is not sufficient to reproduce the deterioration of the tearing modulus, hence a criterion using stress- and strain-based nucleation is established in accordance with the cleavage like fracture process of the intermetallic particle clusters. Not only high

stress triaxiality but also high absolute values of maximum principal stress can be achieved. The decrease of the tearing modulus with aging is also captured successfully by the nucleation model.

Acknowledgements

The authors wish to thank Heikki Suhonen (University of Helsinki), Fabrice Gaslain (Centre des matériaux, MINES ParisTech), Chloé Varenne, Bénédicte Kapusta and Benoît Tanguy (CEA Saclay) for their contributions and the many fruitful discussion. This work was supported by Commissariat à l'Energie Atomique. The ESRF is acknowledged for providing beam time through proposal numbers mi1241, ma2787, in771 (2016) and in1044 (2017).

Appendix A. Atom Probe Tomography

In Figure 17, the long tip (112 million ions, 464 nm long) extracted from the 12 h material demonstrates the intense presence of the hardening precipitation Mg-Si. The step in the middle of the tip is due to microfracture during run. There was an increase in base voltage after the microfracture, and it is not representative of actual shape of sample.

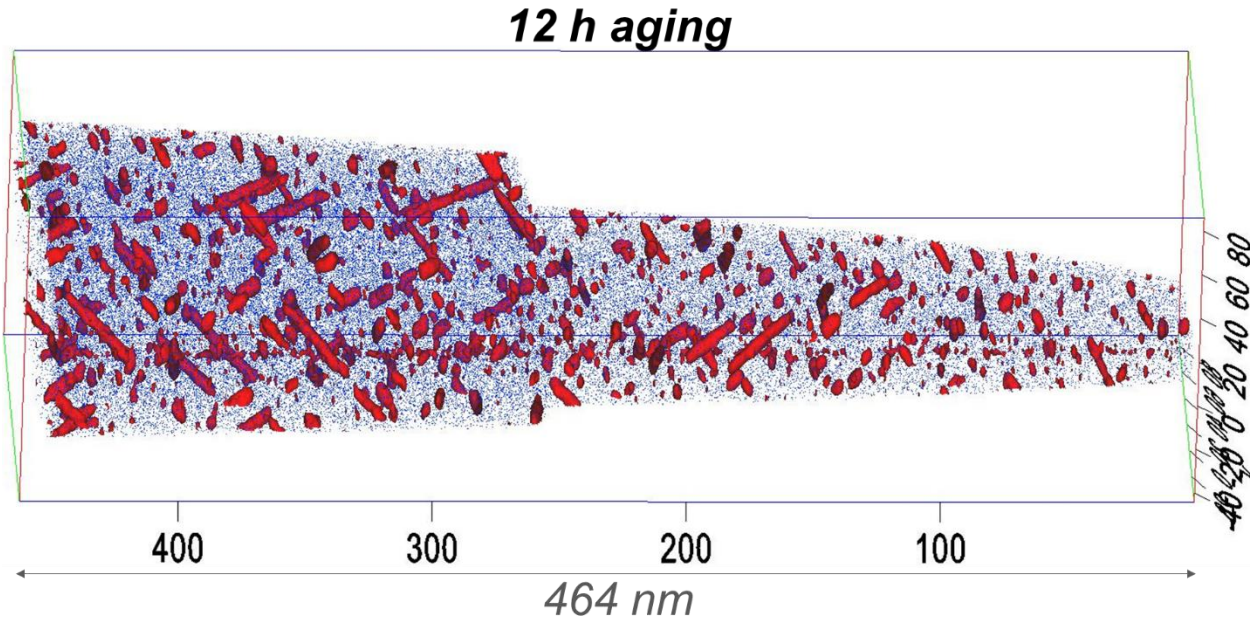


Figure 17 – APT tip after 12 h aging (112 million ions analyzed). The red isosurfaces represent areas of high concentration of Mg (> 3%) in the aluminum matrix represented in blue.

Appendix B. Laminography

The thick specimen is machined in the crack plane of a CT sample after fracture toughness test, which was interrupted after the crack. Therefore, the specimen contains the whole width of the original sample, with lateral notches and the whole crack (Figure 18).

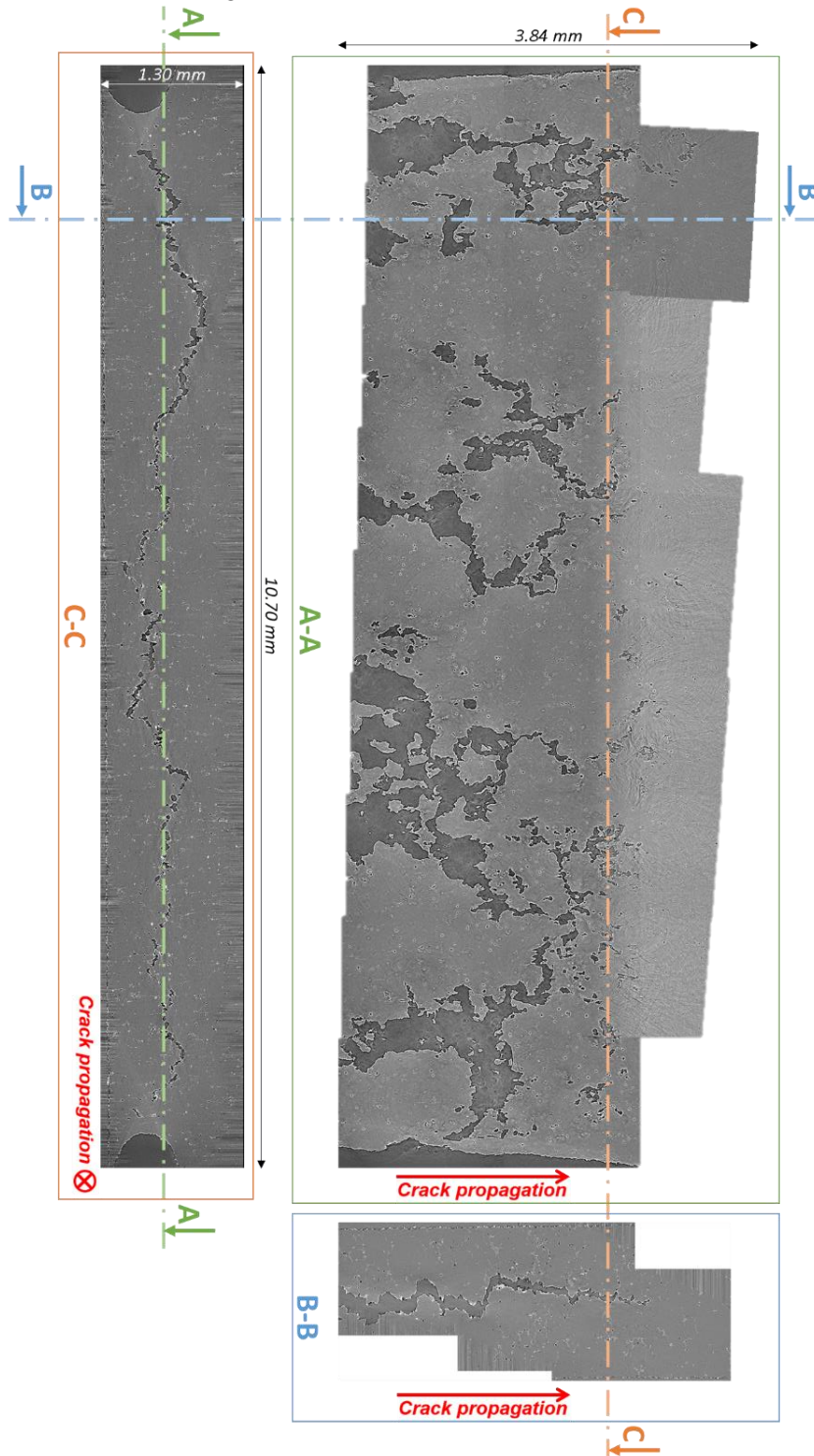


Figure 18 - Recomposition of a section through the entire sample width obtained by sticking 23 laminography scans after 12 h aging.

6. References

- [1] D. Dumont, A. Deschamps, Y. Brechet, On the relationship between microstructure, strength and toughness in AA7050 aluminum alloy, *Mater. Sci. Eng. A*. 356 (2003) 326–336. doi:10.1016/S0921-5093(03)00145-X.
- [2] D. Dumont, A. Deschamps, Y. Brechet, A model for predicting fracture mode and toughness in 7000 series aluminium alloys, *Acta Mater.* 52 (2004) 2529–2540. doi:10.1016/j.actamat.2004.01.044.
- [3] D. Dumont, A. Deschamps, Y. Bréchet, C. Sigli, J.C. Ehrström, Characterisation of precipitation microstructures in aluminium alloys 7040 and 7050 and their relationship to mechanical behaviour, *Mater. Sci. Technol.* 20 (2004) 567–576. doi:10.1179/026708304225016662.
- [4] N. Ryum, The influence of a precipitate-free zone on the mechanical properties of an Al-Mg-Zn alloy, *Acta Metall.* 16 (1968) 327–332. doi:10.1016/0001-6160(68)90018-7.
- [5] N. Ryum, Ageing and plastic deformation of an Al-Mg-Zn alloy, *Acta Metall.* 17 (1969) 821–830. doi:10.1016/0001-6160(69)90101-1.
- [6] G.M. Ludtka, D.E. Laughlin, The influence of microstructure and strength on the fracture mode and toughness of 7XXX series aluminum alloys, *Metall. Trans. A*. 13 (1982) 411–425. doi:10.1007/BF02643350.
- [7] F. Hannard, T. Pardoën, E. Maire, C. Le Bourlot, R. Mokso, A. Simar, Characterization and micromechanical modelling of microstructural heterogeneity effects on ductile fracture of 6xxx aluminium alloys, *Acta Mater.* 103 (2016) 558–572. doi:10.1016/j.actamat.2015.10.008.
- [8] M. de Haas, J.T.M.D. Hosson, On the effects of thermomechanical processing on failure mode in precipitation-hardened aluminium alloys, *J. Mater. Sci.* 37 (2002) 5065–5073. doi:10.1023/A:1021095801205.
- [9] S. Morita, H. Toda, A. Takahashi, A. Hoshiyama, T. Kobayashi, H. Nagashima, Effects of quenching rate on mechanical properties of 6061 aluminum alloy, *J. Jpn. Inst. Light Met.* 51 (2001) 307–312. doi:10.2464/jilm.51.307.
- [10] Y. Shen, T.F. Morgener, J. Garnier, L. Allais, L. Helfen, J. Crépin, Three-dimensional quantitative in situ study of crack initiation and propagation in AA6061 aluminum alloy sheets via synchrotron laminography and finite-element simulations, *Acta Mater.* 61 (2013) 2571–2582. doi:10.1016/j.actamat.2013.01.035.
- [11] T. Petit, C. Ritter, J. Besson, T.F. Morgener, Impact of machine stiffness on “pop-in” crack propagation instabilities, *Eng. Fract. Mech.* 202 (2018) 405–422. doi:10.1016/j.engfracmech.2018.08.007.
- [12] C.C. Chu, A. Needleman, Void Nucleation Effects in Biaxially Stretched Sheets, *J. Eng. Mater. Technol.* 102 (1980) 249–256. doi:10.1115/1.3224807.
- [13] A. Dalloz, J. Besson, A.-F. Gourgues-Lorenzon, T. Sturel, A. Pineau, Effect of shear cutting on ductility of a dual phase steel, *MatModels* 2007. 76 (2009) 1411–1424. doi:10.1016/j.engfracmech.2008.10.009.
- [14] T.F. Morgener, L. Helfen, I. Sinclair, H. Proudhon, F. Xu, T. Baumbach, Ductile crack initiation and propagation assessed via in situ synchrotron radiation-computed laminography, *Scr. Mater.* 65 (2011) 1010–1013. doi:10.1016/j.scriptamat.2011.09.005.
- [15] T.F. Morgener, T. Taillandier-Thomas, A. Buljac, L. Helfen, F. Hild, On strain and damage interactions during tearing: 3D in situ measurements and simulations for a ductile alloy (AA2139-T3), *J. Mech. Phys. Solids*. 96 (2016) 550–571. doi:10.1016/j.jmps.2016.07.012.
- [16] A. Needleman, J.R. Rice, Limits to Ductility Set by Plastic Flow Localization, in: D.P. Koistinen, N.-M. Wang (Eds.), *Mech. Sheet Met. Form.*, Springer US, Boston, MA, 1978: pp. 237–267. doi:10.1007/978-1-4613-2880-3_10.
- [17] C. Butcher, Z. Chen, M. Worswick, A lower bound damage-based finite element simulation of stretch flange forming of Al–Mg alloys, *Int. J. Fract.* 142 (2007) 289. doi:10.1007/s10704-006-9044-3.

- [18] S.J. Andersen, H.W. Zandbergen, J. Jansen, C. TrÆholt, U. Tundal, O. Reiso, The crystal structure of the β'' phase in Al–Mg–Si alloys, *Acta Mater.* 46 (1998) 3283–3298. doi:10.1016/S1359-6454(97)00493-X.
- [19] S.J. Andersen, C.D. Marioara, A. Frøseth, R. Vissers, H.W. Zandbergen, Crystal structure of the orthorhombic U2-Al4Mg4Si4 precipitate in the Al–Mg–Si alloy system and its relation to the β' and β'' phases, *Mater. Sci. Eng. A.* 390 (2005) 127–138. doi:10.1016/j.msea.2004.09.019.
- [20] S.J. Andersen, C.D. Marioara, R. Vissers, A. Frøseth, H.W. Zandbergen, The structural relation between precipitates in Al–Mg–Si alloys, the Al-matrix and diamond silicon, with emphasis on the trigonal phase U1-MgAl2Si2, *Mater. Sci. Eng. A.* 444 (2007) 157–169. doi:10.1016/j.msea.2006.08.084.
- [21] R. Vissers, M.A. van Huis, J. Jansen, H.W. Zandbergen, C.D. Marioara, S.J. Andersen, The crystal structure of the β' phase in Al–Mg–Si alloys, *Acta Mater.* 55 (2007) 3815–3823. doi:10.1016/j.actamat.2007.02.032.
- [22] T.-W. Na, H.-K. Park, C.-S. Park, J.-T. Park, N.-M. Hwang, Misorientation angle analysis near the growth front of abnormally growing grains in 5052 aluminum alloy, *Acta Mater.* 115 (2016) 224–229. doi:10.1016/j.actamat.2016.06.007.
- [23] K. Buchanan, K. Colas, J. Ribis, A. Lopez, J. Garnier, Analysis of the metastable precipitates in peak-hardness aged Al-Mg-Si(-Cu) alloys with differing Si contents, *Acta Mater.* 132 (2017) 209–221. doi:10.1016/j.actamat.2017.04.037.
- [24] S.K. Suram, K. Rajan, Calibration of reconstruction parameters in atom probe tomography using a single crystallographic orientation, *IFES 2012.* 132 (2013) 136–142. doi:10.1016/j.ultramic.2013.02.013.
- [25] L. Helfen, T. Baumbach, P. Mikulík, D. Kiel, P. Pernot, P. Cloetens, J. Baruchel, High-resolution three-dimensional imaging of flat objects by synchrotron-radiation computed laminography, *Appl. Phys. Lett.* 86 (2005) 071915. doi:10.1063/1.1854735.
- [26] L. Helfen, A. Myagotin, P. Pernot, M. DiMichiel, P. Mikulík, A. Berthold, T. Baumbach, Investigation of hybrid pixel detector arrays by synchrotron-radiation imaging, *Proc. 7th Int. Workshop Radiat. Imaging Detect.* 563 (2006) 163–166. doi:10.1016/j.nima.2006.01.085.
- [27] L. Helfen, A. Myagotin, P. Mikulík, P. Pernot, A. Voropaev, M. Elyyan, M. Di Michiel, J. Baruchel, T. Baumbach, On the implementation of computed laminography using synchrotron radiation, *Rev. Sci. Instrum.* 82 (2011) 063702. doi:10.1063/1.3596566.
- [28] A. Myagotin, A. Voropaev, L. Helfen, D. Hänschke, T. Baumbach, Efficient Volume Reconstruction for Parallel-Beam Computed Laminography by Filtered Backprojection on Multi-Core Clusters, *IEEE Trans. Image Process.* 22 (2013) 5348–5361. doi:10.1109/TIP.2013.2285600.
- [29] M. Vogelgesang, T. Farago, T.F. Morgeneuer, L. Helfen, T. dos Santos Rolo, A. Myagotin, T. Baumbach, Real-time image-content-based beamline control for smart 4D X-ray imaging, *J. Synchrotron Radiat.* 23 (2016) 1254–1263. doi:10.1107/S1600577516010195.
- [30] T. Ueda, L. Helfen, T.F. Morgeneuer, In situ laminography study of three-dimensional individual void shape evolution at crack initiation and comparison with Gurson–Tvergaard–Needleman-type simulations, *Acta Mater.* 78 (2014) 254–270. doi:10.1016/j.actamat.2014.06.029.
- [31] T. Weitkamp, P. Tafforeau, E. Boller, P. Cloetens, J.P. Valade, P. Bernard, F. Peyrin, W. Ludwig, L. Helfen, J. Baruchel, Parallel-beam imaging at the ESRF beamline ID19: current status and plans for the future, *AIP Conf. Proc.* 1234 (2010) 83–86. doi:10.1063/1.3463345.
- [32] F. Xu, L. Helfen, H. Suhonen, D. Elgrabli, S. Bayat, P. Reischig, T. Baumbach, P. Cloetens, Correlative Nanoscale 3D Imaging of Electron Density and Elemental Composition in Extended Objects, *PloS ONE.* 7(11) (2012) e50124.
- [33] Y. Shen, Tensile and fracture behavior of AA6061-T6 aluminum alloys : micromechanical approach, Thèse, Ecole Nationale Supérieure des Mines de Paris, 2012.
- [34] F. Hannard, A. Simar, E. Maire, T. Pardoën, Quantitative assessment of the impact of second phase particle arrangement on damage and fracture anisotropy, *Acta Mater.* 148 (2018) 456–466. doi:10.1016/j.actamat.2018.02.003.

- [35] M.W. Zandbergen, Q. Xu, A. Cerezo, G.D.W. Smith, Study of precipitation in Al–Mg–Si alloys by Atom Probe Tomography I. Microstructural changes as a function of ageing temperature, *Acta Mater.* 101 (2015) 136–148. doi:10.1016/j.actamat.2015.08.017.
- [36] W.M. Garrison, N.R. Moody, Ductile fracture, *J. Phys. Chem. Solids.* 48 (1987) 1035–1074. doi:10.1016/0022-3697(87)90118-1.
- [37] E. Voce, The relationship between stress and strain for homogeneous deformations, *J. Inst. Met.* 74 (1948) 537-562.
- [38] V. Tvergaard, A. Needleman, Analysis of the cup-cone fracture in a round tensile bar, *Acta Metall.* 32 (1984) 157–169. doi:10.1016/0001-6160(84)90213-X.
- [39] F.A. McClintock, A Criterion for Ductile Fracture by the Growth of Holes, *J. Appl. Mech.* 35 (1968) 363–371. doi:10.1115/1.3601204.
- [40] G. Rousselier, Ductile fracture models and their potential in local approach of fracture, *Nucl. Eng. Des.* 105 (1987) 97–111. doi:10.1016/0029-5493(87)90234-2.
- [41] A. Gurson, Continuum Theory of Ductile Rupture by Void Nucleation and Growth : Part 1-Yield Criteria and Flow Rules for Porous Ductile Media, *J. Eng. Mater. Technol.* 99 (1977) 2–15.
- [42] V. Tvergaard, Material Failure by Void Growth to Coalescence, in: J.W. Hutchinson, T.Y. Wu (Eds.), *Adv. Appl. Mech.*, Elsevier, 1989: pp. 83–151. doi:10.1016/S0065-2156(08)70195-9.
- [43] J. Besson, Continuum models of ductile fracture : A review, *Int. J. Damage Mech.* 19 (2010) 3–52. doi:10.1177/1056789509103482.
- [44] A. Pineau, A.A. Benzerga, T. Pardoen, Failure of metals I: Brittle and ductile fracture, *Acta Mater.* 107 (2016) 424–483. doi:10.1016/j.actamat.2015.12.034.
- [45] A.A. Benzerga, J.-B. Leblond, A. Needleman, V. Tvergaard, Ductile failure modeling, *Int. J. Fract.* 201 (2016) 29–80. doi:10.1007/s10704-016-0142-6.
- [46] P.F. Thomason, Three-dimensional models for the plastic limit-loads at incipient failure of the intervoid matrix in ductile porous solids, *Acta Metall.* 33 (1985) 1079–1085. doi:10.1016/0001-6160(85)90201-9.
- [47] P.F. Thomason, A three-dimensional model for ductile fracture by the growth and coalescence of microvoids, *Acta Metall.* 33 (1985) 1087–1095. doi:10.1016/0001-6160(85)90202-0.
- [48] A.A. Benzerga, J. Besson, A. Pineau, Anisotropic ductile fracture: Part II: theory, *Acta Mater.* 52 (2004) 4639–4650. doi:10.1016/j.actamat.2004.06.019.
- [49] M.E. Torki, C. Tekoğlu, J.-B. Leblond, A.A. Benzerga, Theoretical and numerical analysis of void coalescence in porous ductile solids under arbitrary loadings, *Int. J. Plast.* 91 (2017) 160–181. doi:10.1016/j.ijplas.2017.02.011.
- [50] M. Gologanu, J.-B. Leblond, J. Devaux, Theoretical models for void coalescence in porous ductile solids. II. Coalescence “in columns,” *Int. J. Solids Struct.* 38 (2001) 5595–5604. doi:10.1016/S0020-7683(00)00355-3.
- [51] F. Hannard, S. Castin, E. Maire, R. Mokso, T. Pardoen, A. Simar, Ductilization of aluminium alloy 6056 by friction stir processing, *Acta Mater.* 130 (2017) 121–136. doi:10.1016/j.actamat.2017.01.047.
- [52] J.A. Walsh, K.V. Jata, E.A. Starke, The influence of Mn dispersoid content and stress state on ductile fracture of 2134 type Al alloys, *Acta Metall.* 37 (1989) 2861–2871. doi:10.1016/S0001-6160(89)80001.
- [53] A.S. Argon, J. Im, R. Safoglu, Cavity formation from inclusions in ductile fracture, *Metall. Trans. A.* 6 (1975) 825. doi:10.1007/BF02672306.
- [54] F. Prat, J. Besson, M. Grange, E. Andrieu, Behavior and rupture of hydrided ZIRCALOY-4 tubes and sheets, *Metall. Mater. Trans. A.* 29 (1998) 1643–1651. doi:10.1007/s11661-998-0087-0.
- [55] Z.. Zhang, C. Thaulow, J. Ødegård, A complete Gurson model approach for ductile fracture, *Eng. Fract. Mech.* 67 (2000) 155–168. doi:10.1016/S0013-7944(00)00055-2.
- [56] J. Besson, L. Devillers-Guerville, A. Pineau, Modeling of scatter and size effect in ductile fracture: application to thermal embrittlement of duplex stainless steels, *Eng. Fract. Mech.* 67 (2000) 169–190. doi:10.1016/S0013-7944(00)00056-4.

- [57] T.J.R. Hughes, Generalization of selective integration procedures to anisotropic and nonlinear media, *Int. J. Numer. Methods Eng.* 15 (1980) 1413–1418. doi:10.1002/nme.1620150914.
- [58] Y. Shinohara, Y. Madi, J. Besson, Anisotropic ductile failure of a high-strength line pipe steel, *Int. J. Fract.* 197 (2016) 127–145. doi:10.1007/s10704-015-0054-x.
- [59] J. Eshelby, The determination of the elastic field of an ellipsoidal inclusion, and related problems, *Proc. R. Soc. Lond. Ser. Math. Phys. Sci.* 241 (1957) 376. doi:10.1098/rspa.1957.0133.
- [60] M. Kroon, J. Faleskog, Micromechanics of cleavage fracture initiation in ferritic steels by carbide cracking, *J. Mech. Phys. Solids.* 53 (2005) 171–196. doi:10.1016/j.jmps.2004.05.008.
- [61] D. François, A. Pineau, A. Zaoui, *Mechanical behaviour of materials. Vol 2 : Fracture mechanics and damage*, Springer, 2013. <https://hal-mines-paristech.archives-ouvertes.fr/hal-00785237>.
- [62] I. Kirman, The relation between microstructure and toughness in 7075 aluminum alloy, *Metall. Trans.* 2 (1971) 1761–1770. doi:10.1007/BF02913403.
- [63] G.T. Hahn, A.R. Rosenfield, Metallurgical factors affecting fracture toughness of aluminum alloys, *Metall. Trans. A.* 6 (1975) 653–668. doi:10.1007/BF02672285.